Chem Soc Rev

Chemical Society Reviews

Gas sensing using porous materials
for automative applications
ZEOLITE | MOF

Themed issue: Sensor targets

ROYAL SOCIETY
OF CHEMISTRY

REVIEW ARTICLE
Andrew D. Burrows *et al*.
Gas sensing using porous materials for automotive applications

Chem Soc Rev

Gas sensing using porous materials for automotive applications

Dominic J. Wales,[a] Julien Grand,[b] Valeska P. Ting,[a] Richard D. Burke,[c] Karen J. Edler,[d] Chris R. Bowen,[c] Svetlana Mintova[b] and Andrew D. Burrows*[d]

Improvements in the efficiency of combustion within a vehicle can lead to reductions in the emission of harmful pollutants and increased fuel efficiency. Gas sensors have a role to play in this process, since they can provide real time feedback to vehicular fuel and emissions management systems as well as reducing the discrepancy between emissions observed in factory tests and 'real world' scenarios. In this review we survey the current state-of-the-art in using porous materials for sensing the gases relevant to automotive emissions. Two broad classes of porous material – zeolites and metal–organic frameworks (MOFs) – are introduced, and their potential for gas sensing is discussed. The adsorptive, spectroscopic and electronic techniques for sensing gases using porous materials are summarised. Examples of the use of zeolites and MOFs in the sensing of water vapour, oxygen, NO_x, carbon monoxide and carbon dioxide, hydrocarbons and volatile organic compounds, ammonia, hydrogen sulfide, sulfur dioxide and hydrogen are then detailed. Both types of porous material (zeolites and MOFs) reveal great promise for the fabrication of sensors for exhaust gases and vapours due to high selectivity and sensitivity. The size and shape selectivity of the zeolite and MOF materials are controlled by variation of pore dimensions, chemical composition (hydrophilicity/hydrophobicity), crystal size and orientation, thus enabling detection and differentiation between different gases and vapours.

1. Introduction

Climate change and the need to combat its associated negative effects constitutes one of the key global challenges of the modern age. It is generally accepted that anthropogenic climate change is largely the result of the production and release of unprecedented levels of greenhouse gases, including carbon dioxide, since the industrial revolution as a result of the combustion of fossil-based fuels such as oil, coal and natural gas.

[a] Department of Chemical Engineering, University of Bath, Claverton Down, Bath, BA2 7AY, UK

[b] Laboratoire Catalyse & Spectrochimie, ENSICAEN, 6 Boulevard Maréchal JUIN, 14000 Caen, France

[c] Department of Mechanical Engineering, University of Bath, Claverton Down, Bath, BA2 7AY, UK

[d] Department of Chemistry, University of Bath, Claverton Down, Bath, BA2 7AY, UK. E-mail: a.d.burrows@bath.ac.uk

Dominic Wales is a Research Officer in the Department of Chemical Engineering at the University of Bath. His project involves the design and application of metal–organic frameworks and zeolites for exhaust gas sensing applications.

Dominic J. Wales

Julien Grand is a Research Engineer in the Laboratoire Catalyse et Spectrochimie (LCS, CNRS), Caen. His project involves the synthesis of new types of zeolites and the development of selective zeolite sensors for automotive exhaust gases.

Julien Grand

Under conditions that allow for complete combustion, carbon dioxide is produced in large quantities. However, under conditions that do not allow for complete combustion, undesired and toxic by-products such as oxides of nitrogen (NO_x), carbon monoxide, sulfur dioxide and various unburnt hydrocarbons are also emitted in smaller quantities, some from impurities present in the fuel.[1] The release of these gases into the atmosphere has resulted in diminished air quality in major cities and built up areas.[2–4] Consequently an increasing amount of research has been directed at the development of technological and materials-based mitigation strategies, for example, the capture and sequestration of CO_2

and methane from the atmosphere. Porous materials, such as activated carbons, zeolites and most recently, metal–organic frameworks (MOFs) have been intensely studied for CO_2 sequestration applications over the last two decades, as their high surface areas and large void volumes make them uniquely suited for adsorptive separation and storage of gases. However, rather than developing these materials for separating and capturing gases, such as CO_2, from dilute mixtures in air ($<1\%$ CO_2) or even from more concentrated flue gases ($\sim 14\%$ CO_2), a more realistic approach could be to employ these materials to reduce the amount of gas emitted at the point of generation.

Valeska Ting is a Lecturer in the Department of Chemical Engineering and the University of Bath's Prize Fellow in Smart Nanomaterials.

Valeska P. Ting

Richard Burke is a Prize Fellow in Automotive Powertrain Systems in the Department of Mechanical Engineering at Bath.

Richard D. Burke

Karen Edler is Professor of Soft Matter at the University of Bath. Her research group works on self-assembly in systems from inorganic surfactant-templated materials, to polyelectrolyte films, nanofibre gels and lipid-polymer particles.

Karen J. Edler

Chris Bowen is Professor of Materials at the University of Bath and ERC Advanced Investigator on Novel Energy Materials, Engineering Science and Integrated Systems (NEMESIS).

Chris R. Bowen

Svetlana Mintova is Director of Research, 1st class at CNRS, Laboratoire de Catalyse et Spectrochimie, ENSICAEN and University of Caen, in Basse Normandy, France.

Svetlana Mintova

Andrew Burrows is a Reader in Inorganic Chemistry at the University of Bath. His research interests lie in functionalised materials with extended structures such as metal–organic frameworks (MOFs).

Andrew D. Burrows

One of the largest contributors to greenhouse gas emissions is the transportation sector, which currently accounts for over a quarter of the total global energy demand worldwide.[5] Between 1990 and 2012, transportation was the second largest source of emitted greenhouse gases in the USA and accounted for 24% of CO_2 emissions in the UK, according to an IMechE report from 2010, with the majority originating from road transport.[3,6] While promising alternative energy technologies (e.g. battery and fuel-cell powered vehicles) are being developed in an effort to reduce future carbon emissions and remove the reliance on fossil fuels, there are many infrastructural and technological hurdles to overcome before these technologies become widespread. Similarly, while mid-term solutions such as the development of biofuels (including bioethanol and biodiesel) offer a lower-carbon alternative to traditional fossil fuels they can still lead to unwanted emissions. The outlook for the next 40 years is that the transportation industry will remain reliant on the internal combustion engine and hydrocarbon-based fuels.[7,8] Hence there is an urgent need for concerted efforts to reduce emissions from transport sources, as well as ensuring that the most efficient use is made of the limited fossil fuel reserves remaining.[9]

1.1 Use of sensors in the automotive industry

The major motivations for the use of sensors to monitor automotive emissions are the legislative requirements to reduce harmful emissions that have negative effects on health and air quality and contribute to global climate change. However, the potential economic benefits from increasing fuel efficiency through reductions in unburnt fuels and increased fuel energy density is also a factor. The greatest gains in developing new multi-functional sensors based on porous materials for the automotive industry are in two main areas: for the design and manufacture of road vehicles, and for use in production vehicles for real-time fuel and emissions management.

1.1.1 Sensors for vehicle design and manufacture. Vehicle design and manufacture is subject to stringent legislative targets in terms of fuel consumption and CO_2 emissions with legislation stipulating a fleet average of 136 g km^{-1} in 2011 with a proposed target of reducing emissions to a 95 g km^{-1} fleet average by 2020.[10] The advent of turbocharging and supercharging technologies, which reduce the engine size and increase the specific power of diesel engines, have also resulted in an increase in the peak cylinder temperatures. This, in turn, results in higher emission levels of NO_x and particulate matter.[11] Carslaw et al. showed that NO_x emissions for modern diesel engines can be twice those of older models, which they attribute to the reduction in engine size.[12]

There is also a need to reduce the discrepancy between emission levels in diagnostic tests used to provide emissions certification in a factory setting (for example on rolling roads using the New European Drive Cycle (NEDC)) and real world emissions, which has become more significant over recent years. As an example, Carslaw et al. used road-side remote sensing equipment to measure real world vehicle NO_x emissions from a large number of vehicles.[12] The results suggested that whilst legislation imposed on factory-tested NO_x emissions

had achieved a reduction from 0.5 g km^{-1} to 0.2 g km^{-1} since the year 2000 (with all new vehicles sold meeting this standard), real world emissions had stagnated at around 1 g km^{-1}.[12] Another review of real world fuel consumption by Mock et al. summarising customer reviews of observed mileage, on-board emissions measurement and laboratory tests, showed that whilst in 2002 the average vehicle had 7% higher fuel consumption on the road compared to the NEDC, in 2012 the difference had increased to 25%.[13] Such studies are motivating the automotive industry to move away from current legislative testing on idealised drive cycles and replace this with more dynamic and representative test cycles.[14] This change presents significant opportunities for emissions sensing. Firstly, replacement drive cycles must be proven to be representative of real world driving and to establish the emissions associated with a real world drive cycle, real data must be captured under representative conditions. This is particularly challenging since current high-accuracy lab-based emissions sampling tends to be a large, intrusive mechanism which cannot be practically deployed on a significantly large scale. Secondly, engine emissions control is primarily achieved indirectly by modelling emissions empirically in order to determine optimum control of different engine features. Without a direct measure of emissions for use as feedback, less accurate indirect control with significant calibration and on-board diagnostics effort is required.[15]

1.1.2 Sensors for on-board fuel and emissions management. For both petrol- and diesel-powered vehicles, the continued tightening of legislated emission limits is increasing the complexity of emissions control systems on engines.[11] In particular, active devices for NO_x and particulate matter rely on an estimation of emissions levels under highly transient conditions and would benefit from a direct, fast and accurate measurement of individual emissions species in real time. Specific active emissions control technologies can already be found on commercially available vehicles and include the use of the following:[15]

(i) Catalytic converters:[16] these reduce emissions of carbon monoxide, unburnt hydrocarbons and NO_x gases. Optimal operation of catalytic converters requires precise control of the concentration of oxygen by the engine management system, in order to tailor the intake air : fuel ratio, known as λ.[17] However, under cold start conditions, in order to raise the temperature of the catalytic convertor, the engine is run in a less fuel-efficient mode, involving higher speed idling, exhaust throttling and over-fuelling.

(ii) Selective catalytic reduction (SCR) catalysts: these reduce emissions of NO_x from diesel engines. Ammonia, as a urea–water solution, is injected into the exhaust stream for the reduction of NO_x into nitrogen and water in the presence of oxygen on the catalyst. The amount of injected urea must be carefully controlled to match the NO_x concentration to ensure full reduction and avoid NO_x emission due to underdosing or ammonia emission from overdosing.

(iii) Particulate filters: exhaust particulates are captured in a ceramic filter, but must be routinely purged by raising the exhaust temperature either by overfuelling or throttling the intake air flow to reduce the particulates.

(iv) Lean NO$_x$ traps: NO$_x$ emissions bind onto barium nitrate coated surfaces when the engine is operating in a lean mode with excess oxygen in the exhaust. When the storage catalyst is full, the engine must induce an oxygen-deprived environment by throttling the engine intakes and operating with a close to stoichiometric air : fuel ratio, to reduce the NO$_2$ into N$_2$ and CO$_2$.

Typically the use of the above technologies will have a detrimental effect on fuel economy either by requiring the injection of additional fuel or the throttling of the engine to control oxygen concentrations and exhaust temperatures. Many modern vehicles powered by an internal combustion engine are fitted with a solid state Zr and Pt-based oxygen sensor and/or a NO$_x$ sensor, which have response times in the order of a few tens of milliseconds.[18,19] However, if the engine management system had access to sensors that could provide real-time information on the concentrations of a larger diversity of products in the exhaust stream, the engine management system could more finely tune the active emissions control, which would be greatly advantageous for increasing engine efficiency.

Thus, there is a need for emissions sensors across a range of applications from high cost, high accuracy research grade analysers for lab-based testing to robust, low cost production-level devices capable of differentiating between a large variety of gaseous species for on-board emissions monitoring. In both of these cases, the different applications will require sensors with different characteristics in terms of the intrusiveness of instrumentation (size, ability to install on vehicles), absolute measurement accuracy, sensor/measurement chain dynamics, feedback and cost.

2. Porous materials for sensing in the automotive industry

There is much potential for the use of porous materials as sensing elements for monitoring and feedback control of the wide variety of gases emitted in vehicle exhausts. The design and tailoring of porous materials for high selectivity allows more sensitive tracking and real-time response to emissions. The large-scale processing of porous materials is established and the production of miniaturised porous-materials sensors is eminently scalable. The vast array of different materials that could be incorporated lends itself to the optimisation of low cost and robust sensors that reduce the need for incorporation of expensive precious metals. In addition, the ability for porous materials to be made into layers of permeable thin films of differently selective materials can potentially be exploited to introduce additional multifunctionality to the final product, allowing a single sensor to detect a wide spectrum of sensing targets.

This review will focus on two major classes of porous materials for sensing applications:

(i) Zeolites, which represent a well-known and industrially relevant class of porous aluminosilicate materials. Zeolites are thermally and chemically robust and made from readily-available and abundant starting materials, which make them attractive for low cost and robust sensors.

(ii) Metal–organic frameworks (MOFs), which constitute a relatively new class of hybrid framework material, consisting of metal nodes connected by organic linkers. These materials have incredible structural diversity and the combination of tailoring metal nodes and organic components to achieve desired interactions is an attractive possibility.

Other classes of porous materials have been used for gas sensing, such as mesoporous silica and metal oxides,[20] carbon nanomaterials[21] and porous silicon.[22] These materials are, however, beyond the scope of this review.

There are several advantages to the use of porous materials in gas sensing applications. Porous materials offer flexibility and versatility in terms of structure and design. Size and shape selectivity for adsorbed species can be imparted to zeolites and MOFs through control of the dimensions of the pores enabling detection and differentiation between the multitude of combustion products in exhaust emissions.[23] In addition the structural flexibility of some frameworks can add a further dynamic dimension to gas selectivity.[24] Chemical selectivity and sensitivity can also be controlled by the incorporation of selected dopants into the zeolite and MOF frameworks in addition to the wide choice of organic linkers and metal nodes that can be incorporated into MOFs.[25–28] Furthermore, MOFs and zeolites can exhibit high temperature stability, i.e. ∼500 °C for some MOF-related zeolitic imidazolate framework materials and ∼1200 °C for some zeolites.[29,30] Indeed, MOFs and zeolites have been utilised as the active sensing element or as a gas selective filter/pre-concentrator in gas sensors which has been noted in several reviews on their applications.[25,26,28,31–35] However, these reviews do not focus on the gases and vapours found in engine exhaust gases; some include examples of dissolved gases and none critically review zeolite- and MOF-based sensors in terms of thermal and selectivity suitability for sensing of gases in exhaust streams.

This review aims to provide an insight into the current state of the art of zeolites and MOFs for the sensing of gases found in vehicle exhausts along with a discussion of the associated sensor technologies allowing them to be employed. The review will also compare and contrast the performance of exemplar porous materials for such applications, to provide a perspective on the future prospects of zeolite- or MOF-based exhaust gas sensors in transportation. Examples of zeolite- and MOF-based sensors for the following important exhaust gases will be examined: water vapour (H$_2$O), oxygen (O$_2$), nitrogen oxides (NO$_x$), carbon monoxide (CO) and carbon dioxide (CO$_2$) together, hydrocarbons (in particular methanol, ethanol, aldehydes and alkanes), ammonia (NH$_3$, the reagent in SCR catalysts), hydrogen sulfide (H$_2$S), sulfur dioxide (SO$_2$) and finally hydrogen (H$_2$). Hydrogen is included due to the potential for it to be employed as an alternative low-carbon fuel for future vehicles. MOFs have been reported as sensing materials for nitroaromatic and nitroalkane vapours. Since these gases are not found in exhaust streams, sensors for these species are not included in this review. However, an excellent review by Banerjee et al. on the sensing of these species was published recently.[36]

This journal is © The Royal Society of Chemistry 2015

Chem. Soc. Rev., 2015, 44, 4290–4321 | 4293

2.1 Zeolites for sensing

Zeolites are defined as crystalline nano- and mesoporous materials with 3D framework structures that form regular and uniform pores and channels. They can be synthesised with different chemical compositions and frameworks which allows for a wide variety of materials; in fact more than 200 known synthetic zeolites have been reported, in addition to 40 natural ones.[37,38] Zeolites consist of tetrahedral units of T (where T is typically Si, Al but can also be another element *e.g.* B, Ga, Ge, or P) bonded by oxygen atoms resulting in a framework containing cages and channels of distinct sizes and shapes. The internal microporosity of zeolites provides high surface areas and active sites for adsorption. In terms of designing zeolites for specific applications, zeolite crystallisation is an important process to control.[39] The nature of precursors, the molar ratios, the type of solvents, the presence or absence of templates and additives or seeds all highly influence the final arrangement of the SiO_4 and AlO_4 tetrahedra. In addition, post-synthesis treatment can be used to tune the obtained properties. Some examples are ion-exchange reactions, surface modification reactions to increase or decrease the hydrophilic character of the zeolite, dealumination reactions to modify the Si/Al ratio of the zeolite framework, tailor the hydrophilic/hydrophobic character and to control the number of cations within the zeolite, and porosity alteration to obtain a hierarchical zeolite which exhibits additional porosity in the mesopore size region.[40]

Molecular sieves are well known for application as adsorption media for various gases, and they can selectively adsorb molecules that are smaller than the pore sizes of the zeolites. Crystalline microporous materials, in particular zeolites, have significant impact in different applications ranging from petroleum refining and petrochemical processes to air separation and nuclear waste management. The completely controlled porous structure of zeolitic materials makes these materials true shape-selective molecular sieves. The presence of charge-compensating cations such as alkali metal, alkaline earth metal and protons within the inorganic frameworks allows fine-tuning of the ion exchange and catalytic properties. The hydrophobic nature of high-silica zeolites or the hydrophilic nature of aluminium-rich zeolites make these solids useful as specific adsorbents of organic molecules or water in the gas or liquid phase. Zeolites are therefore versatile materials in terms of potential applications, and are used as heterogeneous catalysts in industrial processes, ion-exchangers for water purification and water softening, as separating membranes and also as catalyst supports.[41–44]

Furthermore, a number of novel applications depend not only on the control of pore structure and intrazeolite chemistry, but also on the ability to control the morphology and pre-shaping, for example the growth of thin zeolite films for separation and sensing purposes. A number of novel applications of zeolites depend on the ability to create thin films. For numerous synthetic strategies, the main goal is to obtain adhesive layers of zeolites on various substrates such as noble and non-noble metals, glass, ceramics, silicon, and even three-dimensional substrates.[45] The approach employed for a particular zeolite film preparation
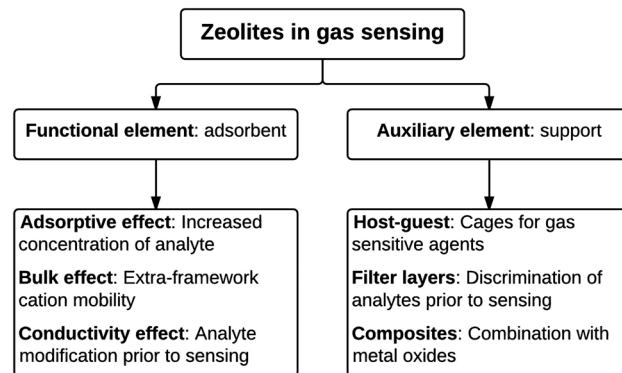

Fig. 1 An overview of the different functions of zeolites in gas sensor applications.

depends on the final application. The porous films can be deposited on the gas-sensitive element in a continuous and crack-free manner. The following three approaches are applied for deposition of zeolite crystals:

(a) spin (dip) coating (thickness in the range of 200–1000 nm)

(b) hydrothermal growth of seeded zeolite layers (thickness of 500–5000 nm)

(c) screen printing based on self-bonded zeolite crystals with/without additives (thickness in the range of 2000–10 000 nm).

In sensing applications, zeolites are used in two main ways, as shown in Fig. 1. Firstly as a functional element with an active role (*e.g.* incorporating a physical response to adsorbed gases) or secondly as an auxiliary element with a supporting role, *e.g.* encapsulating the sensing agent, thereby increasing the concentration of an analyte *via* adsorption or molecular filtering of others gases to improve selectivity or sensitivity of the active sensing agent.

Nine types of zeolite have been reported for sensing in the literature (Table 1) and will be summarised in this review.

In summary, creation of materials with high surface area might allow the selective sensing of gases from exhausts. A porous structure with open accessible volume, high contact surface and strong interactions with only one or more desired analyte would be very important for the design of the required material.

2.2 Metal–organic frameworks for sensing

Metal–organic frameworks (MOFs) are nano- and mesoporous hybrid materials with open 2D or 3D framework structures that contain potential voids. MOFs are composed of metal cations or metal cation aggregates linked by multitopic organic linkers which ultimately assemble into crystalline networks. They can be synthesised from the combination of a variety of di-, tri- and tetravalent cations and many different linkers, and this allows for a huge variety of MOF structures.[132] In addition this large degree of choice of the components in MOFs allows for the design of selective sensing interactions with analyte molecules, based on size or shape exclusion or relative strength of intermolecular interactions. Indeed many types of MOFs have been reported for sensing in the literature.[28,32]

4294 | *Chem. Soc. Rev.*, 2015, **44**, 4290–4321

This journal is © The Royal Society of Chemistry 2015

Table 1 The nine zeolite types reported for gas/vapour sensing. The name and International Zeolite Association three-letter code for each zeolite type is presented. In addition, the representative pore dimensions within the structures are given,[131] along with descriptions of the sensor types and the concentration ranges that were investigated

Framework type	Zeolite	Pore openings (Å)	Analyte/s, sensor type (range)	Ref.
FER	Ferrierite	4.2 × 5.4; 3.5 × 4.8	Carbon monoxide (CO) – conductivity (ppm range)	46
MOR	Mordenite	6.5 × 7.0; 2.6 × 5.7	Water vapour (H_2O) – UV-vis (9–92% RH), nitrogen dioxide (NO_2) – conductivity (ppb range), ethanol vapour (C_2H_5OH) – conductivity (200 ppm) & ammonia (NH_3) – conductivity (ppm range)	47–54
LTA	Zeolite A	4.1 × 4.1	Water vapour (H_2O) – QCM (150 ppm), nitrogen dioxide (NO_2) – QCM (50 ppm), nitric oxide (NO) – QCM (50 ppm), carbon monoxide (CO) conductivity (ppm range), ethanol vapour (C_2H_5OH) – cantilever (25 ppmv), hydrocarbons (HCs) – conductivity (1250 ppm), Metglas (6 ppm) & sulfur dioxide (SO_2) – QCM (50 ppm)	55–70
MFI	ZSM-5 Silicalite-1	5.3 × 5.6; 5.1 × 5.5	Water vapour (H_2O) – cantilever (ng), QCM (250–750 ppm), UV vis (2.8% RH), conductivity (300 ppm), nitrogen dioxide (NO_2) – QCM (200 ppm), carbon monoxide (CO) – impedance (350 ppm), carbon dioxide (CO_2) – calorimetry (ppm range), ethanol vapour (C_2H_5OH) – QCM (50 ppm), cantilever (25 ppmv), IR (16.5 ppm), hydrocarbons (HCs) – conductivity (1250 ppm), IR (22 ppb), Metglas (180 ppm), ammonia (NH_3) – conductivity (5 ppm; 612 ppmv) & hydrogen (H_2) – fibre optic (0.14 nm kPa^{-1})	50–52, 57–61, 66 and 71–93
BEA	Beta	6.6 × 6.7; 5.6 × 5.6	Water vapour (H_2O) – QCM (150 ppm), nitrogen dioxide (NO_2) – conductivity (ppb range), carbon dioxide (CO) – IR (2–100 ppm), ethanol vapour (C_2H_5OH) – conductivity (200 ppm) & ammonia (NH_3) – impedance (25 ppm)	49, 51, 52, 55, 56, 58, 60, 61, 64 and 94–96
FAU	Zeolite X Zeolite Y	7.4 × 7.4 7.1 × 7.1	Water vapour (H_2O) – UV vis (200 ppm), conductivity (40% RH), oxygen (O_2) – UV vis, conductivity (100 ppm), nitrogen dioxide (NO_2) – conductivity (204 ppb), potentiometry (200 ppb), amperometry (ppm range), carbon dioxide (CO) – impedance (1000 ppm), magnetic (0.33%), ethanol vapour (C_2H_5OH) – cantilever (1.4 ppmv), hydrocarbons (HCs) – UV vis (0.06–31.2 µg mL^{-1}), impedance (10 ppm), cantilever (0.7 ppmv), ammonia (NH_3) – conductivity (ppm range) & sulfur dioxide (SO_2) – conductivity (100 ppm)	49–52, 54, 60, 61, 66 and 97–127
STI	Stilbite	4.7 × 5.0; 2.7 × 5.6	Water vapour (H_2O) – conductivity (63% RH), methanol vapour (CH_3OH) & hydrocarbons (HCs) – conductivity (ppm range)	128 and 129
LTL	Perlialite	7.1 × 7.1	Carbon monoxide (CO) – IR (2–100 ppm)	94
AFI	AlPO-5	7.3 × 7.3	Carbon monoxide (CO) – microcalorimetry (ppm range)	130

In a similar way to zeolite materials, the internal microporosity of MOFs provides high surface areas and active sites for adsorption in addition to selectivity provided by the dimensions of the pores. Thus, sensing elements comprised of MOFs can also be used for direct adsorption of and interaction with the analyte of interest or as a support to improve selectivity or sensitivity of the active sensing agent (Fig. 2).

Many different metal–organic frameworks have been reported for sensing in the literature (Table 2) and these will be summarised in this review.

Fig. 2 An overview of the different functions of metal–organic frameworks in gas sensor applications.

2.3 Techniques for monitoring gas interactions

Chemical sensors are miniaturised devices that can deliver real-time and on-line information on the presence of specific compounds or ions in complex samples.[175] In some cases MOFs and zeolites have been used to simply interact with gases and vapours in an irreversible manner and for the purpose of this review this will be referred to as gas detection rather than gas sensing.

When a zeolite or a MOF is used as a functional sensing element with an active role, the real-time gas sensing response can be monitored through (i) mass/mechanical changes, for example *via* a quartz crystal microbalance (QCM), microcantilevers and/or microresonator, (ii) measuring optical property changes (*e.g.* IR spectroscopic measurements, refractive index measurements and/or luminescence spectroscopic measurements), (iii) variation in electric properties (*e.g.* impedance, capacitance and/or resistance), (iv) heat liberation (calorimetry) or even (v) by visible colour change.

Similarly, when the porous material is used as an auxiliary filtering element, the monitoring of the gas absorbance on corresponding sensing agents, such as metal oxides or polymers, can be achieved using the same techniques. The use of the porous materials as hosts for gasochromic sensing agents, such as reactive dyes, allows for visual monitoring in addition to conventional measurements. These monitoring techniques are briefly described below.

Table 2 The metal–organic frameworks reported for sensing of exhaust gases with descriptions of the sensor types and the concentration ranges that were investigated

Metal–organic framework[a]	Analyte/s	Detector/sensor type	Dynamic range (where stated)	Ref.
[Eu(**L1**)(oxalate)$_{0.5}$(H$_2$O)]·2H$_2$O	Water vapour (H$_2$O)	Luminescence quenching	75.8–85% RH	133
[Tb(**L1**)(oxalate)$_{0.5}$(H$_2$O)]·2H$_2$O	Water vapour (H$_2$O)	Luminescence quenching	75.8–85% RH	133
[Tb(tcpto)(H$_2$O)]·2DMF·H$_2$O (PCM-15)	Water vapour (H$_2$O) & ammonia (NH$_3$)	Luminescence quenching	NH$_3$: 4.5–13.4 µmol	134 and 135
[Zn(dpe)(bdc)]·4H$_2$O (ZndB)	Water vapour (H$_2$O)	Luminescence quenching	—	136
[In(OH)(bdc)]	Water vapour (H$_2$O) & ethanol vapour (C$_2$H$_5$OH)	Luminescence spectroscopy	Saturated atmosphere	137
[Zn$_4$O(bdc)$_3$] (MOF-5)	Water vapour (H$_2$O) & ethanol vapour (C$_2$H$_5$OH)	Luminescence spectroscopy	Saturated atmosphere	137
[Cu$_3$(btc)$_2$] (HKUST-1)	Water vapour (H$_2$O), carbon dioxide (CO$_2$), ethanol vapour (C$_2$H$_5$OH), methanol vapour (CH$_3$OH), hydrocarbons (HCs), ammonia (NH$_3$), hydrogen sulfide (H$_2$S) & hydrogen (H$_2$)	Piezoresistive microcantilever sensor (PRMS), colloidal crystal Bragg reflector (CCBR), microcantilever sensor (MCS), Kelvin probe (KP), quartz crystal microbalance (QCM), localised surface polarized resonance (LSPR), surface polarized resonance (SPR) & filter layer on optical sensor (FL)	H$_2$O: 277–1330 ppm (PRMS), 0–8000 ppm (CCBR), 0.2–1.6% (MCS) CO$_2$: measurement at 100 sccm (CCBR), 8–70% (MCS), measurement at 10% (in N$_2$) (QCM), 0–100% (LSPR) C$_2$H$_5$OH: 0–6000 ppm (CCBR), 0.6–2.8% (MCS), 1–70% (SPR), 2–50 ppm (QCM), 2–50 ppm (KP) CH$_3$OH: 1368–6580 ppm (PRMS), 1.2–6.0% (MCS), 1–70% SPR, 25–50 ppm (KP), 10–50 ppm (QCM) HCs: C$_2$H$_6$ = measurement at 100 sccm (CCBR), pentanal 1–15 ppm (KP) NH$_3$: measurement at 5 ppm (KP) H$_2$S: measurement at 2.5 ppm (KP) H$_2$: (FL)	138–147
[Fe$_3$(btc)$_2$] (Basolite® F300)	Water vapour (H$_2$O), ethanol vapour (C$_2$H$_5$OH) & methanol vapour (CH$_3$OH)	Impedimetric gas sensors	H$_2$O: 0–2.5% vol C$_2$H$_5$OH: 7–18% vol	148
[Zn$_4$O(benztb)(btc)$_{2/3}$] (DUT-25)	Water vapour (H$_2$O), ethanol vapour (C$_2$H$_5$OH) & methanol vapour (CH$_3$OH)	Solvatochromism	C$_2$H$_5$OH: 18–35% vol	149
[Fe$_3$O(abdc)$_3$X] (where X = Cl, OH) (NH$_2$-MIL-88B)	Water vapour (H$_2$O) & ethanol vapour (C$_2$H$_5$OH).	UV-visible reflection spectroscopy	—	150
[Ti$_8$O$_8$(OH)$_4$(abdc)$_6$] NH$_2$-MIL-125(Ti)	Water vapour (H$_2$O)	Impedimetric gas sensor	11–95% RH	151
Yb^{3+}@bio-MOF-1, where bio-MOF-1 = [Me$_2$NH$_2$]$_2$[Zn$_8$O(ad)$_4$(bpdc)$_6$]·8DMF·11H$_2$O	Oxygen (O$_2$)	Luminescence quenching	Measurements at 0% and 100%	152
[Zn$_4$O(**L2**)$_2$]·6DMF·H$_2$O	Oxygen (O$_2$)	Luminescence quenching	0.05–1.00 atm P_{O_2}	153
[Cd(**L3**)$_2$(H$_2$O)$_2$]·3DMF·6H$_2$O	Oxygen (O$_2$)	Luminescence quenching	Lower limit 0.50%	154
[Zr$_6$O$_4$(OH)$_4$(bpdc)$_{5.971}$(**L4**)$_{0.029}$] (derivative of UiO-67)	Oxygen (O$_2$)	Luminescence quenching	0.05–0.80 atm P_{O_2}	155
[Zr$_6$O$_4$(OH)$_4$(bpdc)$_{5.942}$(**L5**)$_{0.058}$] (derivative of UiO-67)	Oxygen (O$_2$)	Luminescence quenching	0.05–0.80 atm P_{O_2}	155
[Zr$_6$O$_4$(OH)$_4$(bpdc)$_{5.821}$(**L6**)$_{0.179}$] (derivative of UiO-67)	Oxygen (O$_2$)	Luminescence quenching	0.05–0.80 atm P_{O_2}	155
[Ru$_x$Zn$_{7−x}$(ip)$_{12}$](OH)$_2$ (x = 0.10–0.16) (ruthenium doped MAF-34 MOFs)	Oxygen (O$_2$)	Luminescence quenching	0.03–1.013 bar P_{O_2}	156
[Zn$_4$O(bpz)$_2$(abdc)] (MAF-X11)	Oxygen (O$_2$)	Luminescence quenching	0.05–1.00 bar P_{O_2}	157
[(CH$_3$)NH$_2$][In$_3$O(btc)$_2$(H$_2$O)$_3$]$_2$[In$_3$(btc)$_4$] (CPM-5)	Oxygen (O$_2$)	Luminescence quenching	0.0–1.0 atm P_{O_2}	158
[In$_3$O(OH)(H$_2$O)$_2$(btc)$_2$] MIL-100(In)	Oxygen (O$_2$)	Luminescence quenching	0.0–1.0 atm P_{O_2}	158
Cu-Y(btc), copper doped Y(btc) (JUC-32-Y)	Carbon monoxide (CO)	In situ IR spectroscopy	0–100 ppm	159
[Cu(cbIM)(nIM)] (ZIF-69)	Carbon dioxide (CO$_2$)	Microscale resonator	1300–5200 ppm	160
MV[Mn$_2$Cu$_3$(mpba)$_3$(H$_2$O)$_3$]·20H$_2$O	Carbon dioxide (CO$_2$)	Luminescence spectroscopy	Measurement at 1 bar	161

Table 2 (*continued*)

Metal–organic framework[a]	Analyte/s	Detector/sensor type	Dynamic range (where stated)	Ref.
[Zn(mIM)$_2$] (ZIF-8)	Carbon dioxide (CO$_2$), ethanol vapour (C$_2$H$_5$OH), hydrocarbons (HCs) & hydrogen (H$_2$)	Fabry–Pérot device (FPD), filter layer (FL)	C$_2$H$_5$OH: 0–40% (FPD); HCs: C$_3$H$_8$: 0–100% (FPD); H$_2$: (FL)	162 and 163
[Co(mIM)$_2$] (ZIF-67)	Formaldehyde (HCHO) & methanol vapour (CH$_3$OH)	Interdigitated electrode resistance sensor (IERS)	HCHO: 5–500 ppm CH$_3$OH: measurement at 100 ppm	164
[Zr$_6$O$_4$(OH)$_4$[bdc]$_6$] (UiO-66)	Methanol vapour (CH$_3$OH) & ethanol vapour (C$_2$H$_5$OH)	UV-visible reflectance spectroscopy	CH$_3$OH: 10 µL (vapour) C$_2$H$_5$OH: 10 µL (vapour)	165
[Cu$_2$(OH)(2,2′-bipy)$_2$(btc)]·2H$_2$O	Methanol vapour (CH$_3$OH)	Quartz crystal microbalance	64–160 ppm	166
[Co(4,4′-bipy)](m-bdc)	Methanol vapour (CH$_3$OH)	Quartz crystal microbalance	2–16 ppm	166
[Al$_{12}$O(OH)$_{18}$(H$_2$O)$_3$(Al$_2$(OH)$_4$)(btc)$_6$]·24H$_2$O	Methanol vapour (CH$_3$OH) & ethanol vapour (C$_2$H$_5$OH)	Kelvin probe	CH$_3$OH: 100 ppm (lower limit) C$_2$H$_5$OH: 10–50 ppm	167, 168
[Co$_3$(btc)$_2$]·H$_2$O	Methanol vapour (CH$_3$OH) & ethanol vapour (C$_2$H$_5$OH)	Kelvin probe	CH$_3$OH: 20–50 ppm C$_2$H$_5$OH: 10–50 ppm	167, 168
[Ni$_3$(btc)$_2$]·H$_2$O	Methanol vapour (CH$_3$OH) & ethanol vapour (C$_2$H$_5$OH)	Kelvin probe	CH$_3$OH: 100 ppm (lower limit) C$_2$H$_5$OH: 10–50 ppm	167, 168
[Cd$_3$(btc)$_2$]·H$_2$O	Methanol vapour (CH$_3$OH) & ethanol vapour (C$_2$H$_5$OH)	Kelvin probe	CH$_3$OH: 20–50 ppm C$_2$H$_5$OH: 10–50 ppm	167, 168
[Zn$_2$(ndc)$_2$(dpe)]·2.5DMF·0.25H$_2$O	Methanol vapour (CH$_3$OH), ethanol vapour (C$_2$H$_5$OH) & hydrocarbons (HCs)	Luminescence quenching (LQ)	Concentration of all analytes was vapour pressure of each analytes at room temperature.	169
[Zn$_2$(ndc)$_2$(bpee)]·2.25DMF·0.5H$_2$O	Methanol vapour (CH$_3$OH), ethanol vapour (C$_2$H$_5$OH) & hydrocarbons (HCs)	Luminescence quenching (LQ)	Concentration of all analytes was vapour pressure of each analytes at room temperature.	169
[Zn$_2$(bpdc)$_2$(bpee)]·2DMF (RPM3)	Hydrocarbons (HCs)	Luminescence spectroscopy	—	170
[Zn(NO$_2$-ip)](4-4′-bipy)] (Zn-CID-5)	Methanol vapour (CH$_3$OH)	Quartz crystal microbalance	Measurement at 40%	171
[Co$_3$(tbtc)$_2$(DMF)$_2$]·4DMF	Methanol vapour (CH$_3$OH)	UV-visible spectroscopy and visible colour change	Vapour pressure of methanol at room temperature.	172
[Zn$_2$(tpee)]	Ammonia (NH$_3$)	Luminescence spectroscopy	1% ammonia (NH$_3$) in nitrogen carrier gas	173
[Mg$_2$(dobdc)]	Ammonia (NH$_3$)	Luminescence spectroscopy	1% ammonia (NH$_3$) in nitrogen carrier gas	173
[Cu(att)$_{1.5}$]	Hydrogen sulfide (H$_2$S)	Luminescence spectroscopy	0–650 ppm	174

[a] L^1 = pyridyl-4,5-imidazole dicarboxylate; tctpo = tris(p-carboxylate)triphenylphosphine oxide; dpe = 1,2-bis(4-pyridyl)ethane; bdc = 1,4-benzenedicarboxylate; btc = 1,3,5-benzenetricarboxylate; benztb = N,N,N',N'-benzidinetetrabenzoate; abdc = 2-amino-1,4-benzenedicarboxylate; ad=adeninate; bpdc = 4,4′-biphenyldicarboxylate; L^2 = [Ir(3-(2-pyridyl)benzoate)$_3$]$^{3-}$; L^3 = [Ir[2-(4-carboxylato-2-pyridyl)pyridine-4-carboxylate](2-phenylpyridine)$_2$]$^-$; L^4 = [Ir(6-(4-carboxylatophenyl)pyridine-3-carboxylate)(2-phenylpyridine)$_2$]$^-$; L^5 = [Ir(6-(5-carboxylato-2-pyridyl)pyridine-3-carboxylate)(2-phenylpyridine)$_2$]$^-$; L^6 = [Ru(6-(5-carboxylato-2-pyridyl)pyridine-4-carboxylate)(2,2′-bipyridine)$_2$]$^-$; cbIM = 5-chlorobenzimidazol-1-ate; nIM = 2-nitroimidazolate; mpba = N,N'-1,3-phenylenebis(oxamate); mIM = 2-methylimidazolate; 2,2′-bipy = 2,2′-bipyridine; 4,4′-bipy = 4,4′-bipyridine; m-bdc = 1,3-benzenedicarboxylate; ndc = 2,6-naphthalenedicarboxylate; bpee = 1,2-bis(4-pyridyl)ethylene; NO$_2$-ip = 5-nitro-1,3-benzenedicarboxylate; tbtc = 4-[[3,5-bis[(4-carboxylatophenoxy)methyl]-2,4,6-trimethyl-phenyl]methoxy]benzoate; tpee = tetrakis(phenylcarboxylate)ethylene; dodbc = 2,5-dioxido-1,4-benzenedicarboxylate; att = 3-amino-1,2,4-triazole-5-thiol.

ip = imidazo[4,5-f][1,10]phenanthrolin-1-ide; bpz = 4-(3,5-dimethylpyrazol-1-id-4-yl)-3,5-dimethyl-pyrazol-1-ide; MV = methylviologen dication;

This journal is © The Royal Society of Chemistry 2015

Chem. Soc. Rev., 2015, 44, 4290–4321 | 4297

2.3.1 Detection of mechanical and resonant changes upon adsorption. A quartz crystal microbalance (QCM) transducer consists of a thin slice of a piezoelectric quartz crystal that is used as a sensitive microbalance. The thin section of quartz crystal is electroded and when an AC potential difference is applied to the quartz crystal it oscillates at a specific resonant frequency. Upon adsorption of analyte molecules, the mass increase on the quartz surface is directly related to a reduction in the resonant frequency of the oscillating crystal. Thus, this change in QCM frequency corresponds to the mass of analyte adsorbed, usually on the order of $\sim 10^{-9}$ g cm^{-2}. Selective adsorption of specific analytes is achieved by application of a discriminatory thin film on the surface of the quartz. Further information is available in a review on the use of QCMs for sensing by Vashist and Vashist.[176]

A piezoelectric microcantilever-based transducer uses a similar approach to a QCM transducer but consists of a cantilever paddle that is anchored at one end to a substrate with the other end modified with a sensing material and free to vibrate. When excited by an AC potential difference, the paddle vibrates at its resonance frequency. Upon adsorption of an analyte within or on the sensing layer this specific frequency changes due to mass gain and thus the frequency variation is related to the mass of analyte adsorbed. Further information is available in a review on the use of microcantilevers for chemical sensing.[177] The closely related microresonator-based chemical sensors also operate by adsorption of an analyte leading to a change in mass which in turn changes the resonant frequency of the structure. An excellent paper describing microresonator theory was published by Schmidt and Howe.[178]

A magnetoelastic transducer usually consists of an amorphous ferromagnetic material, in a ribbon form, covered by a sensing film. When an alternating magnetic field is applied, the magneto-elastic material resonates at a specific frequency which changes due to adsorption of an analyte within or on the sensing film. Further information is available in a review on the use of magnetoelastic transducers for sensing.[179]

2.3.2 Spectroscopic sensing techniques. Infrared (IR) spectroscopy for analyte detection can be performed in transmission or reflection mode. In transmission mode, a beam of infrared light is incident to and transmitted by the sensing material. The transmitted intensity *vs.* frequency spectrum of the sensing material is collected periodically and changes in the infrared spectrum corresponding to adsorption of an analyte can be quantified. In contrast, in reflection mode, the sensing material is deposited on a substrate which consists of an optical material with a higher relative refractive index, such as a silicon wafer. A beam of infrared light interacts with the sample due to reflecting times between the bare external surface of the silicon substrate and its internal surface which is in contact with the sensing material. At each reflection an evanescent wave extends into the sample. The monitoring of the transmitted light or the evanescent wave reveals how much energy was absorbed at each frequency. This is described as attenuated total reflection (ATR). In both cases, the properties of the obtained IR spectrum (*i.e.* wavenumber of absorption bands and shape and intensity of bands) is related to the nature and concentration of the analyte interacting with the sensing material.

Optical fibre Bragg gratings can either be long-period gratings or short-period gratings. For both types of optical fibre Bragg grating, the period describes the distance between a fringe of low or high refractive index and the sequential fringe of the same refractive index. Long-period gratings typically have periods on the sub-millimeter length scale and work by coupling forward propagating light of a certain wavelength into forward coupling cladding modes. The coupled wavelength is dependent on the period of the Bragg grating. The power of the forward coupling modes is typically attenuated through absorption and scattering losses. If the cladding of the optical fibre is covered with a sensing material then interaction with analyte species will alter the absorbance, or change the magnitude of scattering losses within the cladding. This can result in a change in the magnitude of the received power at the coupled wavelength at the detector or even a wavelength shift of the transmission peak features. Further information is available in a review on the use of long period Bragg gratings for sensing.[180]

Luminescence-based detector or sensor systems measure changes in the fluorescence or phosphorescence emission spectrum of a luminescent material due to interaction with analyte molecules. Certain molecules, such as dioxygen O_2, quench or "turn-off" the luminescence of the sensing material; the degree of change in luminescent intensity or wavelength shifting is related to the concentration of the quenching analyte.

Optical sensing can be employed if encapsulated reactive dyes are contained inside the zeolite cages. Colour changes caused by the presence of an analyte can be monitored with UV-visible spectroscopy and/or the naked eye.

2.3.3 Electronic sensing. Electrical property-based sensors can be used to monitor the adsorption of analytes within the porous sensing material by measuring changes in conductivity, impedance or resistance of the sensing material upon interaction with an analyte.[181] The change in electrical properties of sensing materials that contain semiconducting metal oxide guests upon exposure to analytes can be monitored in the same manner as the electrical property-based sensors described above. For example, the imaginary permittivity of the sensing material can be correlated to the resonant impedance spectrum or to conductivity.[182]

The different types of sensing and detection techniques used in zeolite and MOF sensors are summarised in Fig. 3.

3. Exhaust gas sensing using porous materials

3.1 Humidity sensors

3.1.1 Zeolite-based H$_2$O sensors. Tracking of water vapour concentration is important for determining the extent of combustion. Early examples of humidity sensors reported the advantages of zeolite-based sensing devices combined with mass detectors. In one of the first examples, ZSM-5 type zeolite single crystals were aligned on a high sensitivity micromechanical

Fig. 3 A comparison of the different types of sensing/detection techniques cited in this review.

cantilever to fabricate a chemical sensor for humidity sensing in the nanogram range.[71] In 2001, other QCM sensors were prepared by modification with either zeolite A or beta polymorph A and used as humidity sensors.[55,56] Due to the large pore size channels (6.7 Å), beta polymorph A-based sensors exhibited more interference from alkanes compared to zeolite A-based sensors. Larger resonant frequency shifts were measured with the zeolite A coated QCM sensor, *e.g.* 2000 Hz after 150 ppm water exposure for zeolite A, compared to 400 Hz for beta polymorph A. However, the response and recovery times were faster for the beta polymorph A zeolite sensor, which was rationalised on the basis of its larger pore channel diameter and higher hydrophobicity due to a higher Si/Al ratio. Other QCM oscillator-based sensors have been developed for humidity sensing, based on zeolite A, silicalite-1 and sodalite deposited onto QCMs, and showed similar results when monitoring from 250 to 750 ppm of water in He at 170 °C.[57] The sodalite-coated QCM was found to be promising as a discriminatory humidity sensor as it showed poor responses towards NO and SO_2.

Host–guest chemistry using zeolites as hosts for a dye or conductive material has also been employed to construct optical or electrochemical detectors and sensors for humidity, respectively. Spectroscopic changes in the nature of the dye loaded into the zeolite cages indicated the presence or disappearance of water. Protonation/deprotonation of methylene blue held in mordenite-type zeolite showed spectral changes in a range of 9 to 92% of relative humidity with good reversibility and fast responses of approximately 2 min for the adsorption step and 4 min for the desorption step.[47,48] Two absorption bands (the monomeric methylene blue and its protonated form at 650 and 745 nm, respectively) were monitored to obtain these results. Another example of an optical humidity detector utilised solvato-chromic Nile Red dye encapsulated in a NaY zeolite.[102] This device had a detection limit of 200 ppm humidity, a response time of around 4 min and discrimination against hexane was also demonstrated. One further example of an optical detector involved impregnation of silver on ZSM-5 type zeolite[72] where the authors showed that Ag^+ species in the Ag-ZSM-5 zeolite exhibited stable optical properties under high-temperature treatment. The behaviour of the 37 700 cm^{-1} band was followed with *in situ* UV-vis spectroscopy. Above 150 °C, this band was found to be sensitive to the presence of water vapour in the gas stream (2.8% H_2O in He), disappearing in the presence of water vapour while full intensity could be recovered under water-free conditions.

As an example of electrochemical sensing, Yu *et al.* employed a porous zeolite support to improve the stability and durability of LiCl at high humidity. Indeed, when the humidity exceeds 40% relative humidity (RH), the conductivity response of LiCl is no longer linear and thus it becomes difficult to use the material as a humidity sensor.[103] The LiCl was dispersed into a NaY zeolite to obtain a linear response to up to 75% RH. The authors claimed that the well-defined cavities of NaY-type zeolites are more suitable as host materials for preparation of humidity-sensitive composite materials than those with channel structure, such as ZSM-5 or mordenite zeolites. Zou *et al.* similarly reported that the loading of LiCl into stilbite resulted in an electrically conductive material exhibiting very high humidity sensitivities with a linear response of 10^4 in conductivity with a humidity change from 0 to 63% and fast response times for adsorption and desorption.[128]

Changes in zeolite conductivity due to extra-framework cations contained in the framework have also been employed for the concept of humidity sensors with measurements based on changes in either impedance or capacitance. The impedance of the H-form of ZSM-5 was studied as a function of water concentration (0–300 ppm) in H_2.[73,74] ZSM-5 zeolite was chosen for its small pore size (5.5 Å), which improved water selectivity, and also for its acidic properties, due to the acid–base chemistry involved in impedance measurements. In addition, the high thermal stability of the zeolite in a reducing environment allowed sensing experiments in H_2 up to 600 °C, measurements which are not possible with humidity sensors based on metal oxides or polymers.

To allow sensing under milder ambient experimental conditions, the capacitance of a zeolite can be measured instead of impedance. For this approach, electrodes coated with various zeolite films (A-, Y-, beta polymorph A- and silicalite-type) with different Si/Al ratios were studied.[58] It was shown that the hydrophilic nature of zeolite A provided the most sensitive film,

This journal is © The Royal Society of Chemistry 2015

Chem. Soc. Rev., 2015, **44**, 4290–4321 | **4299**

with a seven times higher response under a 350 ppm water concentrated atmosphere compared with the other films.

Metal oxide based sensors can be further modified with zeolite films to improve their response to gas analytes compared with uncoated metal oxides. A zeolite layer can be used as an adsorbent filter to enhance the selectivity of the metal oxide by retaining analytes and/or interfering species. An example was reported using SnO_2 as the oxide and zeolite A and ZSM-5 zeolites as filters.[59] Results showed that zeolite A improved the selectivity towards H_2O by the elimination of the response to propane, hydrogen and methane while continuing to respond significantly to ethanol and CO. On the other hand, the ZSM-5-type silicalite-coated sensor gave enhanced response to both H_2O and H_2.

3.1.2 MOF-based H_2O sensors. There have been a large number of reports of different MOF-based humidity detectors and sensors employing a range of analysis techniques due to the variety of interactions of water with the organic moieties or metal centres. For sensing water vapour levels, several research groups have utilised lanthanide-based luminescence, which is sensitive to the chemical environment of the lanthanide ions. Dong et al. developed lanthanide ion MOFs using a mixture of two different ligands: oxalate ($^-O_2C–CO_2{}^-$, ox) and pyridyl-4,5-imidazole dicarboxylate (L^1), and either terbium nitrate or europium nitrate to form $[M(L^1)(ox)_{0.5}(H_2O)]\cdot 2H_2O$ (M = Eu, Tb).[133] Upon dehydration, both MOFs showed a decrease in luminescence emission intensity and upon rehydration the intensity of the luminescence emissions increased again; the MOFs therefore functioned as probes for humidity which could be easily interrogated with luminescent spectroscopic methods. The terbium MOF showed the greatest change in luminescence intensity when the dehydrated form was rehydrated upon exposure to known quantities of water vapour in air, i.e. different relative humidity levels. However, the response time of the terbium MOF probe was slow even in high relative humidity environments. For recovery of the luminescence emission to an intensity equivalent to the luminescence emission intensity of the hydrated form, the dehydrated form had to be exposed to 85% relative humidity (%RH) for 9 h.

Humphrey et al. synthesised a terbium(III) MOF, ([Tb(tctpo)-(H_2O)]·2DMF·H_2O) (DMF = N,N-dimethylformamide), known as PCM-15, with tris(p-carboxylate)triphenylphosphine oxide (tctpo) as the linker (Fig. 4).[135] The resulting MOF is comprised of a 5,5-connected net structure, with each Tb^{3+} centre octa-coordinated, forming seven bonds to tctpo linkers and one to a water molecule. Upon activation of the MOF the intensity of the

photoluminescence due to the terbium ion was found to double. Upon treatment with moisture-saturated N_2, the photoluminescence intensity returned to that for the as-synthesised MOF. Thus, PCM-15 can act as a luminescence-based detector for humidity, though neither the response time nor the luminescence response at different % RH levels were reported. Another MOF which acted as a detector for water vapour was demonstrated by Chou et al.[136] As with the examples above, changes in the luminescence intensity of the MOF upon dehydration and rehydration were used as the measurable output. However this MOF, [Zn(dpe)(bdc)]·4H_2O (dpe = 1,2-bis(4-pyridyl)ethane, bdc = 1,4-benzenedicarboxylate), labelled as ZndB, utilises ligand-based luminescence rather than luminescent lanthanide metal ions. The MOF contains 2D hydrogen-bonded rings of sixteen water molecules and showed reversible on(dry)/off(hydrated) luminescent response to humidity upon cycling between room temperature and 85 °C. The mechanism behind the increase in fluorescence intensity upon heating at 85 °C was thought to be removal of the intra-channel water molecules resulting in a shortening of the inter-channel distance between two dpe moieties. This enhances the π–π stacking between the two interchain dpe moieties and thus increases dpe(π*)–dpe(π) excimer formation. An exposure time of >100 min of the MOF to the ambient % RH level at room temperature was required for the fluorescence intensity to return to as-prepared levels.

Lee et al. also reported two MOFs that can be used to detect humidity by quantifying the differences in the luminescence emission spectra of a MOF when 'wet' and the same MOF when dry.[137] Upon excitation at 270 nm, it was found that for dry [In(OH)(bdc)] emission $\lambda_{max} = 326$ nm and for dry [$Zn_4O(bdc)_3$], MOF-5, emission $\lambda_{max} = 366$ nm.[183] Exposure to water vapour at 40 °C resulted in an emission wavelength redshift of 64 nm for [In(OH)(bdc)] ($\lambda_{max\ water} = 390$ nm) and an emission wavelength blueshift of 27 nm ($\lambda_{max\ water} = 339$ nm) for MOF-5. Therefore, both MOFs act as fluorescent probes for humidity. No reversibility experiments or experiments detailing a fluorescence change upon exposure to different concentrations of water vapour were reported for these MOFs, but they do show reasonable thermal stability, decomposing above 450 °C for [In(OH)(bdc)] and above 400 °C for MOF-5. Such thermal stability would be necessary for a MOF active sensing element for an exhaust gas sensor.[184]

The copper(II) MOF [$Cu_3(btc)_2$] (btc = 1,3,5-benzenetricarboxylate), HKUST-1, has also been used in the development of a piezoelectric cantilever sensor for both humidity and hydrocarbon vapours.[138] Robinson et al. fabricated N-doped piezoelectric microcantilever sensors, ~230 μm long and ~80 μm wide, that were coated with a layer of HKUST-1. The microcantilever sensor device was then activated prior to the start of a sensing experiment by passage of dry nitrogen gas over the device for 15 min at 40 °C. Higher temperatures, required to completely remove adsorbed water, were not possible as the integrity of the device was found to be compromised at temperatures >50 °C at 1 atm pressure. Therefore, the authors waited until a steady state was achieved before sensing experiments were performed. The sensor device was exposed to different concentrations of water in nitrogen gas at 23 °C and at 1 atm pressure. Exposure to
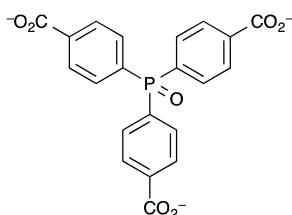

Fig. 4 The tris(p-carboxylate)triphenylphosphine oxide (tctpo) ligand in the Tb^{3+} luminescent PCM-15 MOF prepared by Humphrey et al.[135]

4300 | Chem. Soc. Rev., 2015, **44**, 4290–4321

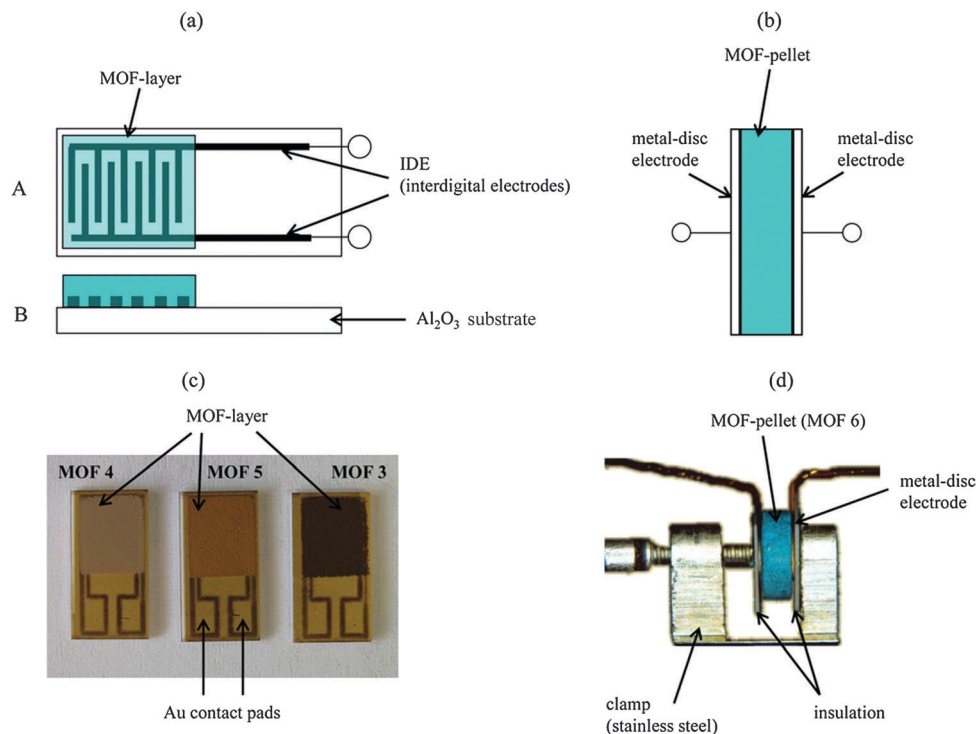This journal is © The Royal Society of Chemistry 2015

Fig. 5 (a) Schematic of the planar interdigital electrode impedance sensor and (c) photographs of the actual planar interdigital electrode impedance sensors covered with thick films of different MOFs by Moos et al.[148] (b) Schematic of the pellet-type metal-disc electrode impedance sensor and (d) photograph of the realised pellet-type metal-disc electrode impedance sensor, by Moos et al., containing a pellet of a MOF.[148] Reproduced under the terms of the Creative Commons Attribution license (http://creativecommons.org/licenses/by/3.0/) from ref. 148 with copyright belonging to the authors of ref. 148.

water vapour resulted in water being adsorbed on the HKUST-1 layer and a change in the resonant frequency of the micro-cantilever. The device demonstrated sensitivity between ∼300 ppm and ∼3000 ppm of water in nitrogen carrier gas and showed sensing reversibility. However, the magnitude of resonant frequency changes that were measured at equilibrium for different concentrations of water vapour in nitrogen carrier gas were identical to those measured upon exposure to different concentrations of methanol vapour. Therefore, based on mea-surable resonant frequency changes, the sensor device cannot differentiate between water and methanol in nitrogen. However, if the response times of the device are taken into account, *i.e.* the adsorption response time and the desorption response time, then analyte differentiation is possible. The adsorption and desorption response times for water were both <30 s, but this was only calculated at one water concentration. Robinson *et al.* defined the response time as the time taken to reach 63.2% of the equilibrium value either during desorption or adsorption as opposed to the definition of gas sensing response time t_{90}, (the time taken to reach 90% of the equilibrium value during adsorption or desorption) that is used more routinely in the literature.[185,186] No sensing results for mixed analyte gas streams were reported. The major disadvantage of this gas sensor in terms of application as a sensor for exhaust gases is the poor thermal instability of the microcantilever.

Impedance humidity sensors that utilise MOFs as the active sensing materials have been developed by Moos *et al.*[148]

The authors investigated two types of impedance humidity sensors; a planar interdigital electrode impedance sensor and a pellet-type metal-disc electrode impedance sensor, both of which are shown in Fig. 5.

For the pellet-type sensor, a pellet of a MOF was placed between the two disc electrodes. For the planar interdigital electrode sensor a thick film of a MOF was deposited on top of the interdigitated electrodes. The authors investigated several MOFs, but found that Fe-btc (Basolite® F300), the iron deriva-tive of HKUST-1, afforded the highest magnitude measured changes in absolute impedance $|\underline{Z}|$, and capacitance C, upon exposure to humidity in a range of 0–3 vol% water in nitrogen carrier gas. Further experiments revealed that the best sensor response in terms of largest magnitude changes in measurable parameters and reversibility was achieved with the planar inter-digital electrode impedance sensor format at the frequency of 1 Hz and with a thick film of Fe-btc MOF as the active sensing material.

At an operating temperature of 120 °C, there was a linear response between $|\underline{Z}|$ and water concentration (in vol%), an overall impedance range of 1.2 GΩ and a sensitivity of 590 MΩ/vol% water, in the range of 0–2.5 vol% water in nitrogen. In addition, the sensor response was reproducible with ∼100% recovery to pre-exposure impedance values after each exposure to water vapour. Therefore this sensor shows promise as a water sensor in exhaust emission sensing applications especially as Fe-btc is thermally stable up to ∼250 °C. However, a disadvantage of

This journal is © The Royal Society of Chemistry 2015

Chem. Soc. Rev., 2015, **44**, 4290–4321 | **4301**

this sensor is that the sensing response becomes non-linear and tends towards exponential at temperatures higher than 120 °C; this limits potential use in hot exhaust gas sensing applications.

As stated above, the large surface areas and high porosity of MOFs allows for the uptake of gaseous analytes and thus favours MOFs as active sensing materials. In addition it is expected that the effective refractive index of the MOF will be sensitive to the uptake of analyte molecules in the pores. Therefore Hupp *et al.* fabricated a refractometric optical-based detector which utilised HKUST-1 as the detection material; adsorption of gaseous analytes in the pores within HKUST-1 changed the effective refractive index of the MOF.[139] The refractometric optical detector consisted of an ordered hexagonal-packed array of sub-micrometer-sized silica microspheres coated in HKUST-1; this is known as a colloidal crystal. A colloidal crystal reflects light at particular wavelengths due to the periodic variation of refractive index within the structure. The reflected wavelength is known as the 'stop band'. At normal incidence the 'stop band' λ_{SB}, in the [111] direction of a colloidal crystal is defined by:[139]

$$\lambda_{SB} = \frac{2\sqrt{2}}{\sqrt{3}} nD \qquad (1)$$

n is the effective refractive index of the colloidal crystal (unitless) and D is the average diameter of the microspheres that make up the colloidal crystal (units = nm). As can be seen in eqn (1), there is a direct relationship between λ_{SB} and n as D remains unchanged; if n increases λ_{SB} also increases and thus redshifts. When Hupp *et al.* exposed the colloidal crystal, modified with HKUST-1 to water vapour at concentrations ranging from 100–12 000 ppm in nitrogen carrier gas, 'stop band' redshifts were measured. The relationship between water concentration and measured 'stop band' wavelength shift was approximately linear between 100–1000 ppm and then plateaued after ~4000 ppm. The authors estimated that the lowest change in concentration of water that could be measured with the device was 2.6 ppm, based on the wavelength resolution of 0.015 nm of the measuring equipment. The detection response was also reversible. However a major limitation of this proof-of-concept device was the MOF was not selective; many different vapours and gases could adsorb onto the MOF which resulted in a change in the effective refractive index of the colloidal crystal. For example, some concentrations of water, methanol and ethanol vapours in nitrogen carrier gas resulted in identical magnitude 'stop band' shifts. One advantage of this device is that it is potentially thermally robust for exhaust gas sensing applications; the silica microspheres were sintered at 600 °C during fabrication of the device and HKUST-1 is thermally stable up to ~250 °C. However, a disadvantage of this current iteration of the detection device is that a light source and a high resolution optical spectrometer are needed to achieve high precision measurements of water vapour. The response of this device to other vapours and gases is discussed in the appropriate sections below.

HKUST-1 was also the chosen active sensing material for piezoelectric microcantilever humidity sensors demonstrated by Hesketh *et al.*[140] The reason for their choice was that small distortions of the HKUST-1 framework occur upon adsorption

of analytes in the pores. If the MOF is in the form of a thin film then the distortion within the framework creates a measurable stress on the piezoelectric microcantilever. The sensor device consisted of a 10-microcantilever array in which each microcantilever incorporated a piezoresistive element. This enabled measurement of changes in stress due to distortion of the framework of the MOF thin film caused by adsorption of analytes. For deposition of the HKUST-1 thin film (~100 nm thick) some of the microcantilevers were coated with gold, which was then modified with a self-assembled monolayer of a thiol; the thiol facilitated the formation of the HKUST-1 thin film on those cantilevers when immersed in the reactant solutions. Some microcantilevers were masked to prevent gold deposition and thus were not subsequently coated with HKUST-1 in order to act as reference microcantilevers. The authors tested the response of the device to water vapour in nitrogen carrier gas with HKUST-1 in either the hydrated as-synthesised state or the 'activated' dehydrated state. The dehydrated state was achieved by passing current through the piezoresistive elements so that temperature reached 50 °C whilst under a flow of dry nitrogen gas for 2 h. It was found that the sensing response to water vapour did not significantly differ whether the HKUST-1 was hydrated or dehydrated. Measurements were performed by exposing the sensor to a flow of water vapour at various concentrations (0–1%) in nitrogen carrier gas at room temperature and pressure. The sensor response was non-linear within the range of water vapour concentrations investigated. The authors reported a measurable change in resistance for adsorption after 0.5 s upon exposure to moist nitrogen gas, though this was the shortest measurement interval used. The time constant for desorption was ~10 s. Fitting of the water resistance curve to a Langmuir isotherm resulted in reasonable agreement with a 0–3 mbar isotherm of water adsorption on HKUST-1, which Hesketh *et al.* state corresponds to a resistance of 7.0 Ω for saturated HKUST-1.[187] The main disadvantage of the sensor was that the HKUST-1 MOF layer did not demonstrate selectivity; methanol and ethanol vapour also adsorbed which resulted in a change in stress. Some concentrations of water, methanol and ethanol vapours in nitrogen carrier gas resulted in identical magnitude measured resistance values. The response of this device to other vapours and gases is discussed in the appropriate sections below.

Fleischer *et al.* also utilised HKUST-1 as the active sensing material for water and other analytes.[141] The device was a Kelvin probe work function-based sensor that consisted of an alumina substrate coated on the top side with a ~2 μm TiN back electrode and a screen printed platinum resistive heater element on the bottom side. On top of the TiN back electrode was a drop cast film of HKUST-1 as the sensing layer (Fig. 6).

Using this Kelvin probe setup, the measured signal represented the difference in the work function of the oscillating gold paddle and the sensing layer. As the gold paddle is not sensitive to the gases used, the signal represents the changes of the electronic structure of the sample under investigation. Humidity sensing measurements were performed in synthetic air (20% O_2 and 80% N_2) at a flow rate of 1 L min^{-1} at 25 °C, and the humidity was studied in the range 0–50%RH. It was

4302 | *Chem. Soc. Rev.*, 2015, **44**, 4290–4321

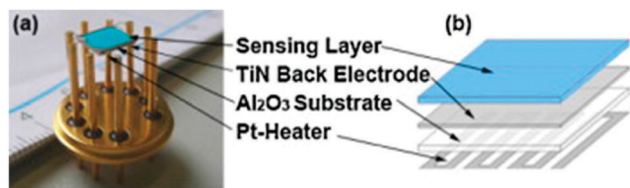This journal is © The Royal Society of Chemistry 2015

Fig. 6 (a) Photograph of the Kelvin probe type sensor fabricated by Fleischer et al. and (b) schematic of the Kelvin probe highlighting the different layers that comprise the device.[141] Reprinted from Sensors and Actuators B: Chemical, 187, Fleischer et al., Work function based gas sensing with Cu–BTC metal–organic framework for selective aldehyde detection, 142–146, Copyright 2012, with permission from Elsevier.

found that the sensing response was reversible and stable with a decrease in work function ($\Delta\phi$) of 5.5 mV per percent increase in relative humidity. In addition it was found that there was only a small influence of variation in humidity on the work function response of the TiN sample; the HKUST-1 layer imparted sensitivity to water vapour. However, the authors also demonstrated the sensitivity of the device to aldehydes and thus the device suffers from cross sensitivity. No response time was given for sensing of water and the thermal stability of the sensor device was also not indicated.

Kaskel et al. reported a mesoporous MOF that acted as a humidity detector.[149] The MOF was the first in a class of MOFs based on the N,N,N',N'-benzidinetetrabenzoate ligand (benztb) (Fig. 7) with auxiliary 1,3,5-benzenetricarboxylate (btc) ligands to strengthen the mesoporous framework.

The particular MOF used in this work was $[Zn_4O(benztb)(btc)_{2/3}]$ (DUT-25) in which two types of pore were found to exist: one mesopore with an internal diameter of 32×20 Å and the other with internal dimensions of 18×8 Å. The BET specific surface area of the MOF was found to be 4670 m^2 g^{-1}. This coupled with the large mesopore means that DUT-25 is suitable for doping with a gasochromic species to enable visual response detecting of gases and vapours. Kaskel et al. loaded the porous structure with the solvatochromic dye Nile Blue and demonstrated that the solvatochromism of the dye was intact despite encapsulation. Upon exposure to water vapour the colour changed from dark blue (due to the presence of Nile Blue in the 'dry' state) to light blue and thus the MOF is a visible indicator material for humidity. The highly porous material could be of interest to developers of exhaust gas sensors based on MOFs as DUT-25 was determined to be thermally stable up to ~ 400 °C in air.

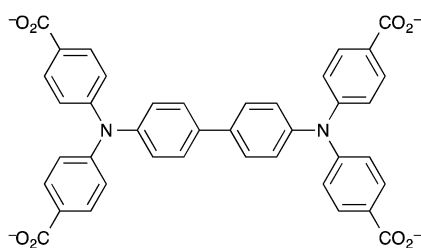Wang et al. have reported a photonic film of a MOF which was used to detect water vapour.[150] Nanoparticles of the iron-based MOF $[Fe_3O(abdc)_3X]$, NH_2-MIL-88B, (X = Cl, OH, abdc = 2-amino-1,4-benzenedicarboxylate) were deposited by spin deposition onto a silicon wafer. The coated silicon wafer was then placed into a quartz cuvette which contained a small volume of water, however the wafer did not come into contact with the water. The UV-visible reflection spectrum of the MOF film was then recorded every 2 min at 20 °C until the reflection spectra became stable. Adsorption of water into the pores of NH_2-MIL-88B replaced air and thus the effective refractive index of the MOF increased. This increase in refractive index resulted in a redshift of the interference peaks in the reflection spectrum by 50 nm. However, greater redshifts were measured upon exposure to hydrocarbon species. These responses are described in Section 3.5.2.

Finally, Ruan et al. have reported an impedance-based sensor for humidity that utilises the MOF $[Ti_8O_8(OH)_4(abdc)_6]$ (NH_2-MIL-125(Ti)).[151] A film of NH_2-MIL-125(Ti) was deposited onto five pairs of Ag–Pd interdigitated electrodes on a ceramic substrate. Upon exposure to relative humidity ranging from 11–95%RH, the largest magnitude change in impedance was measured at 100 Hz. Within this humidity range the impedance decreased from 4.5 MΩ at 11% RH to ~ 124 Ω at 95% RH in a non-linear manner. The t_{90} response time of the sensor, upon increasing concentration of water vapour, was 45 s and the t_{90} recovery time was ~ 50 s.

3.2 Oxygen sensors

3.2.1 Zeolites for O_2 sensing. For O_2 detection and sensing, zeolite-based devices mainly rely on optical host–guest chemistry. For optical oxygen detectors, zeolites have been used as hosts for dyes. Dutta et al. developed a Ru(II) bipyridyl complex as a visual probe which showed a fluorescence (red) in the presence of oxygen contained in macrophage cells.[97,98] They used the supercages of faujasite as holders for the Ru complex to improve its long-term stability and sensing could be carried out under 0 to 1 atmospheres. The faujasite-type zeolite is hydrophobic due to its highly siliceous framework, which enhanced the oxygen transfer from water to zeolite and thus allowed the detection of dissolved oxygen in water with the same Ru complex/zeolite Y sensor.[104]

The supercages of a faujasite-type zeolite have been used to host the dye 2-hydroxymethylanthraquinone for oxygen detection.[99] After photo-activation, the anthraquinone is transformed into oxygen-reactive dihydroxyanthracene, which in the presence of oxygen turns into a coloured anthraquinone allowing the reaction to be followed quantitatively using UV-visible spectroscopy. However, the utility of this detector is limited to one-off oxygen contamination detection by the fact that the reactive dihydroxyanthracene is irreversibly turned into the anthraquinone.

For potentiometric/amperometric O_2 sensing, thin films of zeolites were used to cover conducting sensing electrodes to selectively limit CO_2 exposure of the sensing surface.[105] As the diffusion of oxygen through the zeolite film is preferential to that of CO_2, the coated sensor showed a marked drop in response towards CO_2 along with slightly diminished but still discernable
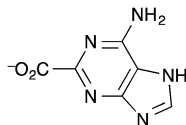

Fig. 7 The N,N,N',N'-benzidinetetrabenzoate (benztb) ligand.

Fig. 8 The adeninate ligand in the **Yb^{3+}@bio-MOF-1** reported by Rosi *et al.* as a potential near-infrared luminescent sensor for oxygen gas.[152]

response towards O_2. A further amperometric and potentiometric bifunctional sensor was developed by Dutta *et al.* which could measure O_2 and NO_2 simultaneously in ppm concentrations.[106] The O_2 and NO_x work by Dutta *et al.* is discussed further in Section 3.3.1.[106]

3.2.2 MOFs for O_2 sensing. Rosi *et al.* reported a MOF for O_2 detection that comprised of zinc metal centres and adeninate ligands which encapsulated and sensitised lanthanide cations in solution. The MOF, $(Me_2NH_2)_2[Zn_8O(ad)_4(bpdc)_6]\cdot 8DMF\cdot 11H_2O$, bio-MOF-1 (ad = adeninate, Fig. 8, bpdc = 4,4'-biphenyldicarboxylate) was used to encapsulate lanthanide cations to form Ln^{3+}@bio-MOF-1. The ytterbium-containing species Yb^{3+}@bio-MOF-1 was then used as a probe for gaseous O_2.[152] The response of Yb^{3+}@bio-MOF-1 to O_2 gas was monitored by measuring the change in intensity of the ytterbium near-infrared luminescence signal at 970 nm, upon excitation with 340 nm light. An approximate 40% decrease in luminescence intensity was observed within the first 5 min of the introduction of O_2 gas to the purged chamber under ambient pressure. After 5 min, the luminescent system reached equilibrium and the intensity of the luminescence remained unchanged during 1 h exposure. Purging the chamber with N_2 resulted in the restoration of the ytterbium near-infrared luminescence to its original intensity even after several cycles of exposure to O_2 and N_2.

$Ir(ppy)_3$ complexes (ppy = 2-phenylpyridine) possess highly efficient phosphorescence owing to the facile intersystem crossing to populate the ^{3}MLCT state. This ^{3}MLCT phosphorescence can be readily quenched by molecules with a triplet ground state such as O_2. Lin *et al.* devised a phosphorescent MOF that consisted of Zn-based secondary building units and ligands that are derivatives of $Ir(ppy)_3$.[153] The linker was a cyclometalated Ir complex based on the 2-phenylpyridine carboxylate derivative **L^2** (Fig. 9).

The porous 2D MOF $[Zn_4O(L^2)_2]\cdot 6DMF\cdot H_2O$ was ground and pressed onto the surface of a KBr pellet, which in turn was placed into a quartz cuvette that was equipped with an inlet/outlet port for O_2 ingress or vacuum. Upon excitation at 385 nm, and after evacuation for 2 h under dynamic vacuum, the luminescence
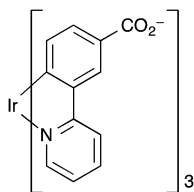

Fig. 9 The iridium(III) metalloligand **L^2** used by Lin *et al.* to fabricate a luminescent MOF for oxygen gas detection.[153]
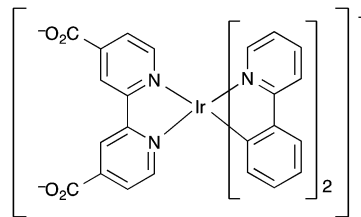

Fig. 10 The iridium(III) metalloligand $[Ir(ppy)_2(dcbpy)]^-$, **L^3**, used in the oxygen sensing MOFs synthesised by Sheu *et al.*[154]

intensity centred at 538 nm decreased upon exposure to O_2 with a sensitivity down to 0.05 atm and quenching efficiency of 59% at 1 atm of O_2. The MOF also demonstrated reversible quenching by O_2 with <5% of the original luminescence intensity lost after 8 cycles with an adsorption response time of ~30 s and a desorption recovery time of ~120 s. The MOF was thermally stable up to ~300 °C.

Sheu *et al.* also used an Ir(III) complex as a ligand to create luminescent MOFs for which the luminescence was quenched in the presence of oxygen.[154] The Ir(III) complex $[Ir(ppy)_2(dcbpy)]^-$ (**L^3**) contains two bidentate 2-phenylpyridine (ppy) ligands and 4,4'-dicarboxy-2,2'-bipyridine (dcbpy) as the third bidentate ligand (Fig. 10). Four MOFs were synthesised by stirring H_2L^3 with the perchlorate salts of zinc(II), cadmium(II), cobalt(II) and nickel(II) in aqueous DMF solution. Of these compounds, the cadmium MOF $[Cd(L^3)_2(H_2O)_2]\cdot 3DMF\cdot 6H_2O$ demonstrated the greatest oxygen detection characteristics with a quenching efficiency of 74% at 1 atm O_2, a linear relationship on the Stern–Volmer plot (ratio of initial emission intensity I_o, to measured emission intensity I, against mole fraction of oxygen χ_{O_2}; I_o/I *vs.* χ_{O_2}) in the χ_{O_2} range 0–1, and the highest Stern–Volmer quenching constant, K_{SV}, at both 1 atm O_2 and at O_2 concentration <0.2 mole fraction. In addition this material had favourable detection kinetics; a 95% response time of 70 s and a 95% recovery time of 30 s. The MOF also showed good reproducibility and the detection response was reversible. Despite the MOF being stable up to ~300 °C, the detection response rapidly deteriorated at temperatures >50 °C. This was ascribed to the loss of co-ordinated guest/free solvent molecules that are involved in the oxygen-detection mechanism.

Lin *et al.* further investigated the use of metal complexes as ligands in three-dimensional MOFs for luminescence-based detection of oxygen.[155] By incorporating the iridium and ruthenium complex ligands **L^4**, **L^5** and **L^6** (Fig. 11) into the zirconium-based MOF $[Zr_6O_4(OH)_4(bpdc)_6]$, UiO-67, *via* a ligand substitution strategy, three phosphorescent MOFs were fabricated.

Nitrogen adsorption/desorption type 1 isotherms at 77 K were obtained for all three of the MOFs and $[Zr_6O_4(OH)_4(bpdc)_{5.971}(L^4)_{0.029}]$, $[Zr_6O_4(OH)_4(bpdc)_{5.942}(L^5)_{0.058}]$ and $[Zr_6O_4(OH)_4(bpdc)_{5.821}(L^6)_{0.179}]$ all had BET surface areas >1000 m^2 g^{-1} indicating microporosity. The MOFs were ground and pressed onto the surface of KBr pellets, which in turn were placed into quartz cuvettes that were equipped with an inlet/outlet port for O_2 ingress or vacuum. Upon excitation at 420 nm, changes in the emission intensity at 600 nm were measured upon stepwise
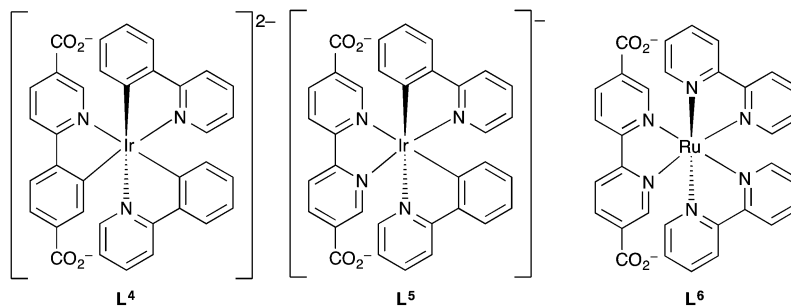
Fig. 11   The phosphorescent metalloligands **L⁴–L⁶** incorporated into UiO-67 by Lin *et al.* for oxygen sensing application.[155]

increase of O_2 pressure starting from vacuum. Decreasing emission intensity with increasing oxygen concentration was observed for the MOFs between 0.001–0.839 atm O_2. The phosphorescence emission of the **L⁵**-based MOF was most efficiently quenched by oxygen with a quenching efficiency of 65% at 0.8 atm O_2. It was found for all three MOFs that the luminescence intensity decreased instantly after initial O_2 concentrations and then much smaller extents of luminescence intensity reduction were observed for the subsequent stepwise O_2 pressure increases. Thus all three MOFs displayed a non-linear response to increasing oxygen concentration which was further demonstrated by the non-linear Stern–Volmer curves. This suggested that the phosphorescent sites were distributed in an inhomogeneous manner within the MOF frameworks. The MOFs displayed reversible, reproducible sensing responses that returned to ~1–3% of the initial intensities even after >5 oxygen sensing cycles.

Chen *et al.* also used the approach of doping a parent MOF framework with phosphorescent ligands to afford a phosphorescent oxygen-detecting MOF.[156] Chen *et al.* chose MAF-34 [$Zn_7(ip)_{12}$](OH)₂ (ip = imidazo[4,5-*f*][1,10]phenanthrolin-1-ide, Fig. 12) as the parent MOF and doped this within varying amounts of ruthenium to form four phosphorescent MOFs of the formula [$Ru_xZn_{7-x}(ip)_{12}$](OH)₂ where x = 0.10–0.16.

The low concentration of the phosphorescent {$Ru(ip)_3$}⁻ units in the MOF meant that self-quenching was avoided. Upon excitation at 480 nm and exposure to increasing oxygen pressure the intensity of the phosphorescent emission at ~600 nm decreased and blueshifted ~5 nm with a very fast response. At 1 atm of O_2 the emission intensities of the MOFs were quenched by between 75 and 88%, the authors attributing the high quenching efficiencies to the ultramicroporous channels within the MOFs and low ruthenium content which leads to more oxygen adsorbed per ruthenium phosphorescent centre. Indeed, high O_2 uptake of 3.2 cm³ g⁻¹ (0.20 mol L⁻¹) was measured at 1 atm and 25 °C.
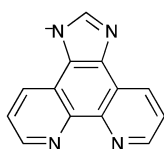
Time dependent luminescence emission profiles, in the absence of oxygen, show biexponential decay characteristics which suggests that the ruthenium phosphorescent centres are in two different environments within the MOFs. This was further confirmed by the non-linear Stern–Volmer plots recorded for all the MOFs, which indicate heterogeneous distribution of the luminescent species. However, a linear response to changing oxygen concentration is measured if a Freundlich adsorption isotherm treatment is applied to the data.

Chen *et al.* fabricated a composite thin film of [$Ru_{0.16}Zn_{6.84}$-(ip)$_{12}$](OH)₂ in silicon rubber on a glass substrate. The thin film demonstrated very fast responses to changing oxygen concentration, good reversibility, reproducibility and stability. In addition, they demonstrated that this composite thin film could be applied to the outside of a commercial blue-light LED which enabled easy identification of changing oxygen concentration with a colour-changing device. The MOF-modified LED emitted magenta light in the presence of N_2, due to the blue emission of the LED combined with the reddish-orange emission of the MOF. In the presence of O_2 the intensity of the reddish-orange emission of the MOF decreased significantly so that the emitted light from the device was violet.

Chen *et al.* have also developed a fluorescent MOF which did not contain any precious metals.[157] [$Zn_4O(bpz)_2$](abdc) (bpz = 4-(3,5-dimethylpyrazol-1-id-4-yl)-3,5-dimethyl-pyrazol-1-ide, Fig. 13), MAF-X11, exhibited fluorescent emission at ~470 nm upon excitation at 345 nm, the intensity of which decreased with increasing oxygen pressure. At 1 bar of O_2, the fluorescence was quenched by 96.5% which is comparable to quenching intensities reported for luminescent hybrid materials containing precious metal complexes. The ratio of initial fluorescent intensity to measured luminescent intensity linearly related to changing pressure of O_2 with a Stern–Volmer constant K_{SV} = 27.1 bar⁻¹. Upon repeated cycling between 1 bar O_2 and vacuum the quenching response was found to be rapid, reversible and highly stable.

Fig. 12   The imidazo[4,5-*f*][1,10]phenanthrolin-1-ide ligand in the ruthenium-doped MAF-34 MOFs of Chen *et al.*[156]
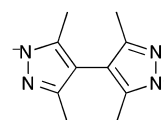

Fig. 13   The 4-(3,5-dimethylpyrazol-1-id-4-yl)-3,5-dimethyl-pyrazol-1-ide ligand in the oxygen sensing fluorescent MOF MAF-X11, reported by Chen *et al.*[157]

This journal is © The Royal Society of Chemistry 2015

Chem. Soc. Rev., 2015, **44**, 4290–4321 | **4305**

Furthermore it was demonstrated that the quenching efficiency of the MOF in air was equivalent to the quenching efficiency at an O_2 pressure of 0.21 bar, thus indicating that the MOF was not cross-sensitive to other gases in air. In addition the MOF was found to be thermally stable up to >450 °C.

Ligand-to-metal energy transfer (EnT) is responsible for the characteristic luminescence of lanthanide MOFs. It has been proposed that the quenching of the luminescence of lanthanide MOFs upon exposure to oxygen gas is due to oxygen deactivating the triplet-state of the organic ligands whilst having very little interaction with the lanthanide ions. For efficient oxygen sensing with lanthanide MOFs, the MOF needs to possess an effective EnT and an appropriate thermally activated energy back transfer (BenT) that will prolong the triplet-state lifetime of the ligands. With this in mind, Qian et al. proposed doping $[(CH_3)_2NH_2][In_3O(btc)_2(H_2O)_3]_2[In_3(btc)_4]$, CPM-5, and $[In_3O(OH)(H_2O)_2(btc)_2]$, MIL-100(In), with Tb^{3+} as they realised that the first triplet-state energy of the btc ligand is $\sim23\,200$ cm^{-1}, which is close to the $^5D_4$ excited state of Tb^{3+} ($\sim20\,400$ cm^{-1}).[158] They proposed that this would result in an effective EnT and appropriate BenT, both of which would be beneficial to oxygen detection. Thin films (~2.5 μm thick) of CPM-5 and MIL-100(In) were grown solvothermally on indium tin oxide glass and then doped with Tb^{3+} by a post-fabrication immersion treatment into an aqueous DMF solution of terbium(III) nitrate to form Tb^{3+}-doped CPM-5 and MIL-100(In) known as CPM-5⊃Tb^{3+} and MIL-100(In)⊃Tb^{3+} respectively. When the luminescent properties of CPM-5⊃Tb^{3+} and MIL-100(In)⊃Tb^{3+} were investigated, it was found that the quantum yield of MIL-100(In)⊃Tb^{3+} was 16.8% which was much larger than the quantum yield of CPM-5⊃Tb^{3+} (1.1%).

Upon exposure to O_2 in a N_2 carrier gas the respective luminescent emissions, at λ_{em} = 544 nm for CPM-5⊃Tb^{3+} and λ_{em} = 546 nm for MIL-100(In)⊃Tb^{3+}, were quenched with a quenching efficiency of 47% at 1 atm O_2 for CPM-5⊃Tb^{3+} and 88% at 1 atm for MIL-100(In)⊃Tb^{3+}. Stern–Volmer plots for the two MOFs showed good linearity suggesting the Tb^{3+} was distributed homogeneously within the MOFs. The Stern–Volmer quenching constant (K_{SV}) for MIL-100(In)⊃Tb^{3+} was an order of magnitude greater than K_{SV} for CPM-5⊃Tb^{3+}. This was ascribed to the greater efficiency of the intramolecular energy transfer within MIL-100(In)⊃Tb^{3+} as opposed to the intermolecular energy transfer within CPM-5⊃Tb^{3+}. Overall the MIL-100(In)⊃Tb^{3+} MOF possessed more desirable properties for O_2 sensing as exemplified by a relatively faster sensing time. It took 6 s to achieve 95% of the maximum reduction in luminescent intensity upon changing from a 100% N_2 atmosphere to a 100% O_2 atmosphere for MIL-100(In)⊃Tb^{3+} and 90 s for CPM-5⊃Tb^{3+}. Upon changing from a 100% O_2 atmosphere to a 100% N_2 it took 53 s for 95% of the maximum recovery in luminescent intensity to be achieved for MIL-100(In)⊃Tb^{3+} and 60 s for CPM-5⊃Tb^{3+}. Furthermore, MIL-100(In)⊃Tb^{3+} exhibited good reversible oxygen quenching and nitrogen recovering properties.

3.3 NOx sensors

3.3.1 Zeolites for NOx sensing. Conductivity measurements are the most developed method for efficient NO_x gas sensing,

usually with conductive metal oxides improved by a zeolite layer working as a filter or induced catalyst. Concerning the use of zeolites as filters, semiconducting WO_3 covered with four different types of zeolite (H-forms of zeolite A, ZSM-5, beta polymorph A and zeolite Y) was investigated as a NO_2 sensor.[60] The best result was obtained with zeolite Y as the covering layer. It exhibited a sensing response to 204 ppb of NO_2 with a response time half that of the bare WO_3 sensor. However, upon exposure to water vapour, the response time increased. More recently, similar results were obtained using ZnO inks as the metal oxide element covered with either zeolite beta polymorph A, zeolite Y or mordenite.[49] Compared to unmodified ZnO sensors, zeolite modification was found to increase the sensitivity of the sensor down to ppb concentrations of NO_2.

In the examples discussed below, the zeolite layer acts as a catalyst prior to sensing in order to maintain a constant composition of the NO_x mixture thus enabling measurement of the equilibration between NO and NO_2 at different temperatures by potentiometry between working and reference electrodes. A NO_x sensor with minimal interferences from CO and O_2 comprised yttria-stabilised zirconia (YSZ) pellets and a Pt-loaded zeolite Y layer.[107] These sensors contain catalytic filters based on YSZ working at temperatures in the range of 300–700 °C. The development of a NO sensor capable of operating in automotive exhaust streams was reported from the same group based on a Pt-yttria-stabilised zirconia (Pt-YSZ) covered by zeolite. The sensors were tested at temperatures between 500 and 700 °C, and the zeolite was permeable to oxygen, thus, was minimising the interference from O_2. The sensor shows interference from CO and NO_2, however these tests indicate that the device is able to detect NO_x in engine exhausts.[109] Using Pt-doped zeolite Y on a yttria-stabilised zirconia electrolyte, the NO_x concentration could be measured using a sensing electrode.[108] This sensor device was then optimised to reduce interference from other gases. The addition of a WO_3 electrode provided the highest reactivity difference with the Pt-doped zeolite Y and interference from 2000 ppm CO, 800 ppm propane, 10 ppm NH_3, as well as the effects of 1–13% O_2, CO_2, and H_2O were minimised.[110,111] A human breath analysis was performed with 20 of those sensors connected in series for the diagnosis of asthma since NO in breath increases from 5–10 ppb (normal state) to 100 ppb in an asthmatic state.[112]

The imbalance in equilibration between NO_2 and NO could also be managed by a voltage change, instead of temperature, to build an amperometric sensor. An example has been reported using the same material, a Pt-doped zeolite Y on a yttria-stabilised zirconia, connected to a potentiostat.[113] It demonstrated a ppm detection of NO_x with no interference from CO and hydrocarbons. Both amperometric and potentiometric monitoring were combined to build a bifunctional sensor which could measure NO_2 and O_2 simultaneously in ppm concentration with almost no interference between each other.[106]

A QCM oscillator-based sensor was also developed for NO sensing that took advantage of the adsorption of NO on zeolites. Zeolite A, silicalite-1 and sodalite were deposited on a QCM and NO adsorption was followed. The zeolite-A doped QCM was

4306 | Chem. Soc. Rev., 2015, 44, 4290–4321

This journal is © The Royal Society of Chemistry 2015

shown to be suitable for monitoring 50 ppm of NO in He at 443 K.[57]

Another approach involves preparation of sulfur-resistant bimetallic noble metal layers, where Cr and W improve the sulfur resistance of Pd–Y zeolite (FAU-type framework structure). On the other hand, La, Mn, Mo and Ag make the sulfur resistance worse and the second metal had no evident influence on product selectivity and the acidic properties of the catalysts. In all of these cases the metals were introduced by ion exchange, and the metal clusters tend to agglomerate with time and migrate to the surface of the sensing layers.[188]

Sensor protection in a destructive thermal and chemical environment was ensured by depositing a porous absorption material around the gas-sensitive section. A zeolite-type material or boehmite was introduced in the sensor substrate with additives and binders and subjected to thermal treatment up to 700 °C. The protective layers were stable at the described working conditions.[189] Protective hydrophilic layers were prepared to prevent water from interfering with the operating sensors. These layers were based on highly hydrophilic materials such as zeolites A, X, and Y.[68]

It is notable that no examples of MOFs for NO_x sensing could be found in the literature at the time of writing. However, NO adsorption in MOFs has been reported by Morris and co-workers for biological applications,[190–193] suggesting MOFs that possess suitable stability for automotive exhaust gas sensing hold promise as potential sensing materials for NO.

3.4 CO and CO_2 sensors

3.4.1 Zeolites for CO/CO_2 sensing. The detection of CO and CO_2 is a major target for vehicular emissions sensing. CO adsorption is usually assessed by conductivity measurements, either from metal oxides encapsulated within the zeolite or in a polymer–zeolite composite. For CO_2, examples include polymer–zeolite composites or zeolites directly grown or deposited on the sensing element. One of the first examples of a metal oxide in a zeolite for sensing was the combination of a sensing layer of La_2O_3-Au/SnO_2 ceramic and a layer of siliceous ferrierite-type zeolite which acted as an ethanol catalytic filter.[46] Indeed, the acidic nature of the zeolite converted ethanol into ethane to reduce the sensitivity of the ceramic towards ethanol and thus improve sensitivity to CO. The ferrierite coating afforded a ten times enhanced sensitivity towards CO at 300 °C. Semiconducting tungsten oxide and chromium titanium oxide covered with zeolite have also been found to be sensitive to CO, but have been reported as more efficient materials for NO_2 and ethanol sensing, respectively, as described herein.[60,61]

With respect to conductive polymer and zeolites for CO sensing, two composites have been investigated. Firstly, a polyaniline/zeolite A-type zeolite sensor has been developed which exhibited high selectivity towards CO, especially with the Ca^{2+} form of the zeolite.[62] Indeed, Ca-zeolite A possesses larger pores than the K^+ and Na^+ analogues and thus does not greatly influence the diffusion of CO through the conductive polymer.[69] The second example reported the utilisation of poly(3,4-ethylenedioxythiophene) doped with polystyrene sulfonic acid and ZSM-5.[75] The sensitivity of the composite increased when the Si/Al mole ratio of the zeolite decreased. However, this composite only produced irreversible responses.

Under a CO reductive atmosphere, the reversible redox behaviour of TiO_2 clusters within Y-type zeolite pores was followed by *in situ* UV-vis spectroscopy providing an efficient CO detector.[114] The zeolite matrix permitted good stability of the clusters towards several oxidation–reduction cycles. In comparison with bulk TiO_2, the TiO_2–Y composite showed 10 times faster response times, of about 1 s at 800 °C.

As an alternative to conductivity measurements, a calorimetric sensor has been developed that measures the heat liberated during the catalytic reaction occurring in Pd-doped zeolites.[63] Combined with a thin-film calorimeter, Pd-zeolite A exhibited a selective response towards CO over alkanes such as n- and i-butane, cyclo- and n-hexane.

Recently, Pd-containing perlialite and beta polymorph A zeolite films showed high molecular recognition towards CO through *in situ* IR spectroscopy.[94] Fast detection of 2 to 100 ppm concentration of CO in the presence of highly concentrated vapours of methanol or pentane (400–4000 ppm) has been demonstrated. Similar results were obtained using a Pt-containing beta polymorph A zeolite film for CO detection in the presence of a highly concentrated methanol atmosphere.[95]

A convenient gas sensor combining a solid electrolyte NASICON, lithium carbonate and a NaY-type zeolite as filter has been reported for air quality control through CO_2 sensing.[115] The fabricated sensor was found to be stable over two years and could follow the CO_2 concentration *via* impedance measurements. For example, when CO_2 exposure increased from 350 to 1000 ppm, the response time was about 2 min. More recently, the NASICON was replaced with sodium conductive ZSM-5 zeolite which provided higher selectivity towards CO_2.[88] The zeolite layer works as both a catalyst and filter due to its sodium cation conductive activity and its well-defined small pore sizes. Conductive-based CO_2 sensing has also been demonstrated using a polymer poly(aniline)–zeolite Y composite.[194] This sensor showed good ability for CO_2 sensing at room temperature.

A composite made of a zeolite Y film grown on a Metglas magnetoelastic strip has also been developed for CO_2 sensing in a N_2 atmosphere.[195] Indeed, when an alternating current magnetic field is applied, the specific resonant frequency showed a discernable decrease down to a concentration of 0.33% CO_2 in N_2. However, a dry atmosphere is required to avoid interference with water as 2% relative humidity affected measurements. A similar device was subsequently reported using silicalite-1 thus permitting the sensing of CO_2 in air instead of a N_2 atmosphere.[76]

Microcalorimetric devices can now be made using lithographic techniques. One of the two sensitive areas of such a device (where evolved heat can be measured) was coated with a thin film of $CoAlPO_4$-5, the other was kept open as a reference.[130] The additional benefit of a zeolite with catalytic activity for such a device is the molecular sieving effect that can be combined in the response of the sensor (a molecule too big to enter the catalytically active interior of the zeolite should only show a weak response). The change in temperature was measured with

This journal is © The Royal Society of Chemistry 2015

Chem. Soc. Rev., 2015, **44**, 4290–4321 | 4307

Fig. 14 Schematic of the layout of the *in situ* IR reactor cell and IR *operando* gas detection experimental set-up used by Mintova *et al.* for detection of carbon monoxide.[159] Reprinted with permission from X. Zou, J.-M. Goupil, S. Thomas, F. Zhang, G. Zhu, V. Valtchev and S. Mintova, *J. Phys. Chem. C*, 2012, **116**, 16593–16600. Copyright 2012 American Chemical Society.

a meandering Pt-wire resistor. This device was examined for the detection of CO and cyclohexane, and sensitivity and selectivity in the low ppm range was observed.

3.4.2 MOFs for CO/CO$_2$ sensing. Mintova *et al.* described a Cu–Y(btc) MOF that was selective to carbon monoxide over water and some hydrocarbons.[159] The yttrium-based MOF [Y(btc)], JUC-32-Y, was doped with copper clusters to afford sensitivity to carbon monoxide. Before sensing of gaseous analytes, nano-crystals of Cu–Y(btc) were deposited onto silicon wafer substrates using a dip coating technique. Before detection of carbon monoxide, the thin films were treated *in situ* within the IR spectrometer gas detection set-up (outlined in Fig. 14) with 5% hydrogen in argon at 300 °C for 9 h to reduce the Cu^{2+} ions to Cu^0 and some Cu^+_n species, which was monitored with UV-visible spectroscopy and confirmed by X-ray diffraction.

The IR spectral changes of the thin films of Cu–Y(btc) due to exposure to a range of concentrations of CO (1–100 ppm) were monitored *in operando* at room temperature. The adsorption of CO on the Cu^0 metal clusters resulted in the appearance of an IR absorption peak centred at 2114 cm^{-1}; the area of this peak could be quantified and related to the concentration of CO present in the Ar carrier gas. Remarkably a concentration as low as 1 ppm of CO in Ar can be detected by measuring the change in absorption at 2114 cm^{-1} and the detection was reversible, albeit requiring a purge of Ar gas for 4 h at room temperature. Additionally the MOF is thermally stable up to $\sim$500 °C and selectively detected CO over water, which was always present at a concentration of $\sim$100 ppm in the Ar carrier gas, and to vapours of chloroform and 2-ethylthiophene that were deliberately introduced. The MOF also showed reproducibility with no diminished response after 10 sensing cycles.

The piezoelectric microcantilever humidity sensor, modified with HKUST-1, demonstrated by Hesketh *et al.* (Section 3.1.2) also displayed sensitivity to carbon dioxide.[140,142] The authors

tested the response of the device to CO$_2$ in nitrogen carrier gas at room temperature and pressure with HKUST-1 in the dehydrated state. The sensor response was non-linear within the range of water vapour concentrations investigated, $\sim$10%–$\sim$70% concentration. However, when HKUST-1 was in the hydrated state no response to carbon dioxide was observed. The authors postulated that the removal of water molecules coordinated to the copper centres was required for carbon dioxide to bind.

The refractometric optical-based detector which utilised HKUST-1 as the sensing material, fabricated by Hupp *et al.* (Section 3.1.2), displayed limited sensitivity to carbon dioxide.[139] Upon exposure to carbon dioxide the measured 'stop band' redshift was $\sim$3 nm relative to N$_2$. The device also displayed sensitivity to other analytes other than water vapour, thus isolation of carbon dioxide from other exhaust gases and vapours would be required.

Candler *et al.* utilised zeolitic imidazolite framework (ZIF) nanoparticle-couple microresonators to sense carbon dioxide.[160] The silicon microresonators were coated with particles of [Zn(cbIM)(nIM)] (cbIM = 5-chlorobenzimidazol-1-ate, nIM = 2-nitroimidazolate, Fig. 15), ZIF-69, by dielectrophoresis. The resonator structure was then exposed to various concentrations of CO$_2$ at room temperature and the change in resonant frequency of the microresonator relative to the anchor was measured with a laser Doppler vibrometer set-up. A linear response was observed between the change in relative frequency and concentration of CO$_2$ in the range 0–4000 ppm. At 5200 ppm of CO$_2$ it was determined that 72 times more CO$_2$ was adsorbed onto the ZIF-69 coated microresonator than on the bare silicon microresonator, thus highlighting the value of increasing the surface area for gas adsorption and thus enhancing the sensitivity of gas sensors. The sensor was cross-sensitive to isopropanol vapour, but differentiation was possible when the decay constant of the adsorption times were compared. The lowest mass change that was measureable and thus the lower detection limit of the sensor set-up was calculated to be $\sim$26 fg.

Duyne *et al.* utilised a localised surface plasmon resonance (LSPR) spectroscopic approach to detect the interaction of carbon dioxide with triangular silver nanoparticles that had been coated with HKUST-1.[143] Upon exposure to CO$_2$ a redshift in the localised surface plasmon resonance wavelength was measured due to adsorption of CO$_2$ within the MOF and thus increase of the refractive index of the MOF-coated silver nanoparticles. The measured redshift in the LSPR wavelength for the device coated with HKUST-1 coated silver nanoparticles was 14 times greater than for the device coated with bare silver nanoparticles. The sensor device displayed a dynamic range in the concentration range 0–100% CO$_2$ in N$_2$ carrier gas and the sensing responses were reversible and reproducible over 5 cycles.
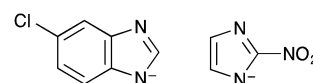

Fig. 15 The 5-chlorobenzimidazol-1-ate (cbIM) and 2-nitroimidazol-3-ate (nIM) ligands in ZIF-69.
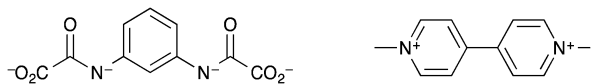
4308 | *Chem. Soc. Rev.*, 2015, **44**, 4290–4321

This journal is © The Royal Society of Chemistry 2015

Fig. 16 (left) N,N′-1,3-phenylenebis(oxamate) tetraanion and (right) methylviologen dication.[161]

Pardo *et al.* demonstrated a detector for carbon dioxide based on the two-dimensional MOF MV[Mn$_2$Cu$_3$(mpba)$_3$(H$_2$O)$_3$]·20H$_2$O (MV = methylviologen dication and mpba = N,N′-1,3-phenylenebis-(oxamate), Fig. 16), which is both magnetic and luminescent.[161] Upon excitation at 400 nm, exposure to 1 bar carbon dioxide or a 1.5 bar 1:1 mixture of carbon dioxide and methane, a luminescent wavelength redshift of 17 nm was measured indicating an interaction of CO$_2$ but not methane with the MOF. It was shown that the MOF was sensitive to both water and methanol in toluene. The authors predict that differentiation of carbon dioxide from both water and methanol would be possible as methanol and water exposure resulted in an emission wavelength blueshift whereas an emission wavelength redshift was measured upon exposure to carbon dioxide.

3.5 Hydrocarbon and volatile organic compound sensors

3.5.1 Zeolites for sensing hydrocarbons and volatile organic compounds.
Tracking of unburnt hydrocarbons and volatile organic compounds (VOCs) is important for determining the extent of combustion. The first example of VOCs and hydrocarbon sensing used a silicalite-1 film on a QCM for ethanol sensing. Monitoring the ethanol adsorption showed a lower limit response at 50 ppm.[196] However, since this work in 1992 no further exploitation of the QCM sensor format has been reported. Indeed, the most frequent zeolite-based hydrocarbon sensors rely on conductivity measurements. An early example of Pt-doped faujasite-type zeolite deposited as a thin film on an inter-digital capacitor was used as a butane sensing material by measuring its impedance response to alternating current excitation.[100] At about 350 °C, a 10 ppm concentration of butane gas could be detected with a time response of 1 s.

As described in Section 3.1.1, sensors have been prepared using SnO$_2$ with zeolite A- and ZSM-5-type zeolites as filters.[59] Results showed that the SnO$_2$/zeolite A sensor responded significantly to ethanol vapour along with improved selectivity towards H$_2$O by the elimination of the response to hydrocarbons (propane and methane). Pd-doping of the SnO$_2$/zeolite A sensor improved the selectivity against hydrocarbons as only 1250 ppm of propane provided any response.[53,70] The water adsorbed by the hydrophilic zeolite A blocked the ingress of propane and any propane that did ingress was subsequently oxidised on Pd.

Another example reported the use of silicalite-1 on SnO$_2$ for the sensing of ethylene in the presence of water, where the zeolite layer acted as a filter to improve selectivity towards hydrocarbons.[89] The [010] oriented zeolite layer gave improved response and recovery time (14 s, 144 s) compared to a randomly oriented zeolite layer (25 s, 208 s). This was rationalised on the basis of vertical channels of the silicalite-1 permitting the concentration of ethylene faster than with randomly orientated silicalite-1.

Recently, a Si cantilever was used to detect toluene and ethanol vapours down to ∼25 ppmv in air.[54] The adsorbent layer consisted of either organophilic silicalite or hydrophilic zeolites A and Y. To remove the adsorbed species from the nanoporous structure and thus improve performance, the hydrophilic zeolite-coated cantilevers were degassed at high temperature. Therefore, zeolite Y cantilevers with integrated heaters have been developed and could detect 1.4 ppmv of ethanol and 0.7 ppmv of toluene in air.

Semiconducting chromium titanium oxide covered with different types of zeolite (H-forms of zeolite A, ZSM-5, beta polymorph A and zeolite Y) have also been investigated as ethanol sensors.[61] The highest sensitivity was obtained with the zeolite Y-modified sensor; the sensing response was doubled compared to a bare sensor. Computational studies showed that the improved sensitivity was due to a catalytic reaction and diffusion behaviour within the zeolite. Two semiconducting metal oxides (tungsten and zinc) covered with zeolite have also been described as ethanol sensors, but it has been reported that the cross-sensitivity to NO$_2$ was significant (Section 3.3.1).[49]

Using two semiconducting tungsten and chromium titanium oxide sensors covered with the acidic form of zeolite A, it was reported that ethanol could be discriminated from isopropanol.[64] Computational studies indicated that this discrimination was due to size and shape selectivity afforded by the zeolite A layer. Earlier, an electrical impedance study took advantage of the shape-selectivity of zeolite channels using natural stilbite zeolite for the discrimination of methanol, 2-propanol and 3-pentanol against water and 2,2-dimethylpropanol.[129] Additionally, a study on the electrical conductivity response of three different zeolites (ZSM-5, mordenite and zeolite Y) towards ethanol was reported.[50] The effects on sensing response of the framework structure, the nature of the charge balancing cation (NH$_4^+$ or H$^+$ forms) and the hydrophilic/hydrophobic character due to Si/Al ratio were investigated. The sensitivity decreased with the increase of the Si/Al ratio and ammonium forms of zeolites gave negative responses whereas all H$^+$ forms gave positive responses. The H$^+$-zeolite Y with a Si/Al ratio of 30 provided the highest electrical conductivity sensitivity to ethanol vapour.

Another possibility for alcohol and hydrocarbon sensing is the use of a conductive polymer combined with zeolites. Two polymers combined with the K$^+$ form of zeolite A were investigated. Both polypyrrole and polypyrrole–polyamide-6 composite sensors exhibited sensitivity towards acetone, methylether ketone, methanol and toluene.[65] Interestingly, this study showed that the preparation of composites influenced the results, as pellets and films were found to be vapour sensitive whereas electrospun fibre bundles were insensitive. However, in the case of methanol sensing, the role of the zeolite remained unclear as the sensitivity could also be explained by the interaction between methanol and polyamide-6.

A silicalite-1–Metglas composite originally developed for CO$_2$ sensing in air (see Section 3.4.1) was found to efficiently discriminate linear and branched hydrocarbons.[76] It selectively detected *n*-butane while it did not respond to the presence of i-butane. Recently, a new study concerning zeolite–Metglas

This journal is © The Royal Society of Chemistry 2015

Chem. Soc. Rev., 2015, **44**, 4290–4321 | 4309

composites was reported for hydrocarbon sensing.[66] It was found that a faujasite-based composite exhibited the lowest detection limits for *o*-xylene at just 6 ppm but suffered of a lack of selectivity with cross-sensitivity to *p*-xylene. On the other hand, a zeolite A-based sensor showed high selectivity between xylene isomers. Concerning *n*-hexane sensing, the best sensitivity (180 ppm) was obtained using the randomly-oriented ZSM-5-zeolite/Metglas sensor.

A composite comprised of zeolite Y cages as hosts for C_{60} has also been developed.[116] Two types of composites, C_{60}/zeolite Y and K-C_{60}/zeolite Y, were deposited onto tantalum comb-type electrodes providing semiconductor sensors. In the presence of ethylene, the composites exhibited measurable changes in conductivity. Similarly, the zeolite ZSM-5 was used as a host for Pt clusters on two electrodes, Au and Cr, in order to build a propane-sensitive detector in the presence of $O_2/CO_2/N_2$.[77] The catalytic oxidation of propane in the presence of Pt and O_2 resulted in a reversible drop in potential.

The conductivity induced by the mobility of extra-framework cations can also be measured by impedance or potentiometry methods. Impedance response towards hydrocarbons has been reported using a Cr_2O_3 layer on top of an ion-conducting Pt-doped ZSM-5.[78] The device showed low interference to CO and H_2, but no selectivity with NH_3. Several studies by the same group were carried out to elucidate the mechanism of the sensing. It was found that the interfacial effect between Cr_2O_3 and Pt-doped ZSM-5 on the electrodes led to the selectivity of propane and propylene and that the impedance response was influenced by the presence of hydrocarbons at low frequencies.[79] Two explanations were proposed to explain the impedance variation. On one hand, the presence of hydrocarbons might act as a charge density carrier with the Cr_2O_3 layer providing the impedance changes.[197] On the other hand, the sorption of hydrocarbons could lead to the insertion of Na^+ from the zeolite to the Cr_2O_3 layer which then led to the formation of sodium chromate at the interface providing the impedance changes.[198]

Potentiometric measurements between a reference Au/Na_2CO_3 electrode and a measuring electrode, comprised of $BaCO_3$/ZSM-5/Au, have been studied for propane sensing at 400 °C.[80,81] The differential between Na^+ activity in the reference and Na^+ activity in the ZSM-5 zeolite was monitored.[82] The highest sensitivity was obtained using a high Si/Al ratio within the zeolite and time responses were improved by the use of films instead of pellets.[67] More recently, the design of a planar potentiometric gas sensor based on Pt-doped zeolite films was envisaged by the same group.[199]

Catalytic reactions inside zeolite cages have also been developed for detection of hydrocarbons. As many zeolites possess acid sites, they can easily promote cracking reactions of C_7–C_{10} linear alkanes. This property was exploited using Cr-zeolite Y and Mo-zeolite Y coated on semiconducting chromium titanium oxide.[117,118] Using Cr-zeolite Y, nonane could be discriminated from heptane, octane and decane by producing a distinct response due to its catalytic transformation into methylpropanol and water. Using Mo-zeolite Y, linear alkanes provided mainly acetaldehyde along

with water and ketones. Even if the discrimination and/or sensitivity was not high, an interesting point is that the sensing was monitored by the products of the catalytic reaction instead of by the analytes themselves.

A catalytic reaction was also used to increase selectivity to propane over propylene. A Pt-doped ZSM-5 layer covering semiconducting $SrTi_{0.8}Fe_{0.2}O_3$ suppressed the propylene response while the propane was selectively detected.[83,84] However, the mechanism of the suppression remains unclear. Pt was also used to dope zeolite Y which was then mixed with semiconducting TiO_2.[119] The obtained Pt-doped zeolite Y/TiO_2 composite showed selectivity towards propane over CO. It was suggested that the propane oxidation catalysed by Pt-zeolite Y produced water which then interacted with TiO_2 providing a resistance change which was monitored.

Optical measurements can also be performed. Adsorption within the zeolite increases the analyte concentration and thus enhances the sensitivity of the optical detector device. One example exploited the adsorption of *n*-hexane in silicalite-1 to provide a 180 times enhanced signal compared with an uncoated ATR element.[90] The refractive index can also change due to the presence of the analyte. For example, when silicalite-1 was coated onto a long period fibre grafting detection limits of 16.5 ppm of isopropanol and 22 ppb of toluene were measured.[91] However, the response time was faster for isopropanol than for toluene due to its smaller size; isopropanol undergoes a faster equilibration within the zeolite structure.

A different approach utilised the light emission obtained by the reaction of acetaldehyde with oxygen atoms in the zeolite cages.[120] Followed by cataluminescence, the signal showed a linear response for 0.06–31.2 µg mL^{-1} acetaldehyde vapour. In addition, acetaldehyde could be discriminated from other aldehydes due to structural constraints within the zeolite; no response was measured with methanol, ethanol, isopropanol, toluene, chloroform, dichloromethane and acetonitrile.

An optical detector based on light emission upon detection of linear alkanes such as *n*-hexane which used a CsNaY zeolite has been developed.[121] The catalytic activity has been explained by zeolite basicity which might enhance the formation of a four-membered ring transition state involving a carbonium ion and oxygen atom. The detection of linear alkanes was demonstrated down to a 0.55 µg mL^{-1} concentration limit with minor interference from alcohols and aromatics. In addition, linear alkanes could be discriminated from branched alkanes due to structural constraints within the zeolite under more concentrated atmospheres (3.88 µg mL^{-1}).

3.5.2 MOFs for sensing hydrocarbons and volatile organic compounds. The refractometric optical-based detector which utilised HKUST-1 as the active sensing material, fabricated by Hupp *et al.* (Section 3.1.2), also displayed sensitivity to vapours of ethanol, ethane and ethylene.[139] Upon exposure to ethanol vapour at concentrations ranging from 100–12 000 ppm in nitrogen carrier gas, 'stop band' redshifts were measured. The relationship between ethanol vapour concentration and measured 'stop band' wavelength shift was approximately linear between 100–1000 ppm and then plateaued after ∼4000 ppm. It was

4310 | *Chem. Soc. Rev.*, 2015, **44**, 4290–4321

This journal is © The Royal Society of Chemistry 2015

estimated that the lowest change in concentration of ethanol vapour that could be measured with the device was 0.3 ppm. The sensitivity limit to ethanol vapour was lower than that for water vapour due to the higher relative refractive index of ethanol. However, a major limitation of this proof-of-concept device was the MOF was not selective; different concentrations of water and ethanol vapours in nitrogen carrier gas resulted in identical magnitude 'stop band' shifts. The device demonstrated limited sensitivity to ethane and ethylene gases in nitrogen carrier gas. The measured 'stop band' redshifts were ~ 5 nm and ~ 6 nm relative to the 'stop band' wavelength in N_2 for ethane and ethylene respectively.

Hupp *et al.* also reported a ZIF-8 based Fabry–Pérot device as a selective sensor for propane and ethanol vapours.[163] Adsorption of ethanol or propane into the pores of $[Zn(mIM)_2]$ (mIM = 2-methylimidazolate), ZIF-8, replaced nitrogen and thus the effective refractive index of the MOF increased. The increase in refractive index due to exposure to either ethanol or propane vapour resulted in a redshift of the interference fringes in the transmission spectrum. The response of the system to propane in nitrogen gas in a concentration range 0–100% was linear with a maximum interference fringe redshift of ~ 50 nm measured in 100% propane. The device was unresponsive to sterically bulkier cyclohexane. In addition, the response of the system to ethanol vapour in nitrogen gas in a concentration range 0–100% was non-linear with a maximum interference fringe redshift of ~ 60 nm measured in 40% ethanol with no further interference redshift occurring at concentration of ethanol vapour $>40\%$.

The Kelvin probe sensor setup demonstrated by Fleischer *et al.* (Section 3.1.2) was also sensitive to aldehydes.[141] Aldehyde vapour sensing measurements were performed in synthetic air (20% O_2 and 80% N_2) at a flow rate of 1 L min^{-1} at 25 °C, and at 40% RH. The sensing response was reversible and stable with changes in work function ($\Delta\phi$) measured upon exposure to the vapours of individual aldehydes. The change in work function upon exposure to 10 ppm of acetaldehyde and propanal were -1 mV and $+1.4$ mV respectively whereas the device was more sensitive to pentanal with a change in work function of -5 mV upon exposure to just 2 ppm. The device suffered from limited cross sensitivity with differences in the measured work function upon exposure to just pentanal, pentanal with acetaldehyde and pentanal with propanal.

Lee *et al.* reported two MOFs that can also be used to detect ethanol by quantifying the differences in the luminescence emission spectra before and after exposure to ethanol vapour.[137] Upon excitation at 270 nm, it was found that for dry $[In(OH)(bdc)]$ emission λ_{max} = 326 nm and for dry MOF-5 emission λ_{max} = 366 nm. Upon exposure to ethanol vapour the profile of the emission peak of $[In(OH)(bdc)]$ changed from a single peak to a triple peak emission feature with $\lambda_{max\ EtOH}$ = 389 nm. However in the case of MOF-5 the emission wavelength blueshifted 27 nm to $\lambda_{max\ EtOH}$ = 339 nm, which was an identical to the $\lambda_{max\ water}$ value. Therefore MOF-5 was not able to differentiate between water and ethanol vapours.[184]

Robinson *et al.* fabricated N-doped piezoelectric microcantilever sensors, ~ 230 µm long and ~ 80 µm wide, that were coated with a layer of HKUST-1 (Section 3.1.2).[138] The sensor device was exposed to different concentrations of methanol vapour in nitrogen gas at 23 °C and at 1 atm pressure. Exposure to methanol vapour resulted in methanol being adsorbed onto the HKUST-1 layer, changing the resonant frequency of the microcantilever. The device demonstrated sensitivity between ~ 1000 ppm and $\sim 13\,000$ ppm of methanol vapour in nitrogen carrier gas and demonstrated a reversible sensing response. However, the magnitude of changes in voltage that were measured at equilibrium for different concentrations of methanol vapour in nitrogen carrier gas were identical to those measured upon exposure to different concentrations of water vapour. The sensor device was however able to differentiate between water and methanol vapour by taking into account response times.

The piezoelectric microcantilever humidity sensor modified with HKUST-1, demonstrated by Hesketh *et al.* (Section 3.1.2), also displayed sensitivity to vapours of ethanol and methanol.[140] The authors tested the response of the device to methanol and ethanol vapours in nitrogen carrier gas, at room temperature and pressure, with the HKUST-1 in both the dehydrated and hydrated state. The sensor response to both ethanol and methanol vapours was non-linear within the range of ethanol vapour concentrations (up to $\sim 2\%$) and methanol vapour concentrations (up to $\sim 8\%$) investigated. Whether the HKUST-1 was in the hydrated or dehydrated state made no discernible difference to the response for both alcohols.

The mesoporous MOF $[Zn_4O(benztb)(btc)_{2/3}]$ loaded with Nile Blue, reported by Kaskel *et al.*, also was a detector for vapours of ethanol and methanol.[149] Upon exposure to ethanol and methanol vapours the colour changed from dark blue (due to the presence of Nile Blue in the 'dry' state) to light blue.

The planar interdigital electrode impedance sensor coated with a thick film of Fe-btc MOF and operating at a frequency of 1 Hz, reported by Moos *et al.* as a humidity sensor (Section 3.1.2), was also sensitive to methanol and ethanol vapours.[148] At an operating temperature of 120 °C, there was a linear response between absolute impedance $|Z|$ and concentration of either methanol or ethanol in the range of 0–35 vol% methanol vapour in nitrogen and 0–18 vol% ethanol vapour in nitrogen. However, after exposure to either methanol or ethanol vapour, a longer desorption time was required for the sensor to return to the pre-exposure impedance value relative to water vapour. In addition, a drifting impedance value was observed upon repeated exposures to ethanol vapour.

The photonic film of NH_2-MIL-88B MOF on a silicon wafer was also sensitive to ethanol vapour.[150] Adsorption of ethanol into the pores of NH_2-MIL-88B replaced air and thus the effective refractive index of the MOF increased. This resulted in a redshift of the interference peaks in the reflection spectrum by ~ 300 nm.

Zhang *et al.* reported that the MOF $[Co(mIM)_2]$, ZIF-67, acted as a selective and highly sensitive sensing material for formaldehyde at 150 °C.[164] ZIF-67 was coated onto silver–palladium interdigitated electrodes and the resistance of the MOF was measured during exposure to various analytes at 150 °C. The highest response was observed upon exposure to formaldehyde,

This journal is © The Royal Society of Chemistry 2015

Chem. Soc. Rev., 2015, **44**, 4290–4321 | **4311**

but there was slight cross-sensitivity to methanol and acetone vapours. The response of the sensor to ammonia vapour and methane was negligible. The sensor was shown to be sensitive to formaldehyde in the concentration range 5–500 ppm with a linear sensing response between 5–50 ppm of formaldehyde. ZIF-67 is stable up to 250 °C in air.

Huo et al. reported that self-assembled crystals of a MOF can be used for optical detection of methanol and ethanol vapours.[165] Particles of $[Zr_6O_4(OH)_4(bdc)_6]$, UiO-66, were modified with poly-vinylpyrrolidone and then films on the surface of a surfactant solution were formed using the Langmuir–Blodgett technique. These films were then transferred to a silica substrate using a dip coating technique. The thin films of self-assembled crystals of UiO-66 were then put into a quartz cuvette that was placed into a UV-visible spectrometer. Adsorption of ethanol or methanol into the pores of UiO-66 replaced nitrogen and the refractive index of the thin film changed. This caused the colour of the photonic crystal thin films to change. A redshift of the absorption peak by 30 nm occurred upon exposure to methanol vapour. This change in colour due to exposure to methanol vapour was also visible to the naked eye.

Zhao et al. reported two MOFs, $[Cu_2(OH)(2,2'-bipy)_2(btc)]\cdot 2H_2O$ and $[Co(4,4'-bipy)(m-bdc)]$ (2,2'-bipy = 2,2'-bipyridine; 4,4'-bipy = 4,4'-bipyridine; m-bdc = 1,3-benzenedicarboxylate), which were highly sensitive to methanol vapour at room temperature when deposited as films on QCM sensors.[166] When the QCM sensor coated with $[Cu_2(OH)(2,2'-bipy)_2(btc)]\cdot 2H_2O$ was exposed to methanol vapour it exhibited an approximately linear response with larger magnitude negative frequency shifts with higher concentrations of methanol vapour. The response time was approximately on the order of 1–2 min and the responses were reversible. The QCM sensor coated with $[Co(4,4'-bipy)(m-bdc)]$ was also exposed to methanol vapour and it exhibited a non-linear response with larger magnitude negative frequency shifts with higher concentrations of methanol. Both MOFs had relatively poor thermal stability, degrading at 170 °C or below.

The techniques of surface plasmon resonance sensing and imaging, using HKUST-1 as the active sensing element, for the detection of straight chain alcohols was reported by Chen et al.[144] Crystals of HKUST-1 were self-assembled from solutions of the reactants using a stepwise-immersion protocol onto a layer of gold, the surface of which had been modified so as to have terminal alcohol groups present. The polarisation of the surface plasmon mode was found to have a linear relationship with concentration of both ethanol and methanol vapour in the range 1% to 70% (v/v), although the sensor was overall more sensitive to methanol than ethanol. The response of the sensor was reversible and highly reproducible.

Urban et al. also used MOFs based on the btc ligand as the active sensing elements on a work function based sensor.[167,168] The design and operation of the sensor was similar to the water vapour sensor reported by Hesketh et al. (Section 3.1.2) and the MOFs investigated were $[Al_{12}O(OH)_{18}(H_2O)_3\{Al_2(OH)_4\}(btc)_6]\cdot 24H_2O$, $[Co_3(btc)_2]\cdot H_2O$, $[Ni_3(btc)_2]\cdot H_2O$ and $[Cd_3(btc)_2]\cdot H_2O$. Upon exposure to methanol or ethanol vapour at different concentrations in synthetic air carrier gas, at 25 °C and at 40% RH, the work function was found to decrease insignificantly for methanol and only marginally for ethanol vapour. The largest response was measured with the work function sensor modified with the layer of $[Cd_3(btc)_2]\cdot H_2O$. However, upon repeating the experiment in dry synthetic air (i.e. 0% RH), the work function decreased more significantly for both methanol and ethanol. In both cases the largest sensor response was measured upon exposure to ethanol vapour, however differentiation between the two alcohols in a mixed vapour stream would be difficult as the magnitude change in work function upon exposure to methanol at ~ 50 ppm was identical to that upon exposure to ethanol at ~ 10 ppm. Additionally, the sensor device showed cross sensitivity to other alcohols such as 2-propanol and n-butanol. Upon exposure to straight chain alkanes slight changes in measured work function were measured, but only in dry conditions. In all cases the sensing responses were reversible.

Work by Pohle et al. compared the response of this work function-based sensor to the response of a QCM sensor upon exposure to vapours of alcohols.[145] Both sensors were modified with films of Cu-btc and exposed to different concentrations of methanol and ethanol vapours under different conditions. For both sensor types it was found that operation in dry conditions resulted in the largest measureable responses to methanol and ethanol vapour. In addition, it was found that the largest changes in frequency response from the QCM-based sensor were measured upon exposure to methanol vapour rather than ethanol vapour. In contrast, methanol vapour caused the smallest work function changes measured with the work function-based sensor compared to ethanol vapour. Therefore, if both sensors were operated at the same time, then two-dimensional discrimination of the nature of the analyte could be achieved.

Li et al. measured the change in fluorescence intensity and the wavelength shift of the fluorescence peak for two MOFs upon exposure to the vapours of many different organic compounds and then plotted these data onto a two-dimensional detection map which allowed differentiation between all of the analytes.[169] The MOFs employed were $[Zn_2(ndc)_2(dpe)]\cdot 2.5DMF\cdot 0.25H_2O$ and $[Zn_2(ndc)_2(bpee)]\cdot 2.25DMF\cdot 0.5H_2O$ (ndc = 2,6-naphthalene-dicarboxylate; bpee = 1,2-bis(4-pyridyl)ethylene). $[Zn_2(ndc)_2(bpee)]\cdot 2.25DMF\cdot 0.5H_2O$ displayed the larger responses to analytes in terms of fluorescence intensity change and fluorescence peak wavelength shift after exposure to the vapour of the analyte at room temperature for 5 min. The two-dimensional detection response map allowed for facile differentiation between methanol and ethanol. In addition it was found that both MOFs were stable up to ~ 400 °C in a nitrogen atmosphere.

An orientated film of a fluorescent MOF on a glass substrate has been reported as a luminescence-based detector of alkenes by Balkus et al.[170] $[Zn_2(bpdc)_2(bpee)]\cdot 2DMF$, RPM3, was grown solvothermally on a glass substrate, the surface of which had been seeded with zinc oxide particles. The resulting film of RPM3 was ~ 3 μm thick and had grown preferentially in the crystallographic c-axis direction. Interestingly the thin film format of the MOF seemed to introduce stability to relative humidity compared to RPM3 powder. The MOF thin film was then doped with silver cations. The presence of Ag^+ within the

MOF partially quenched the fluorescence intensity at ∼422 nm due to the π–cation interaction with the bpee ligand. Upon exposure to propylene gas in dry nitrogen carrier gas the fluorescence intensity was enhanced by ∼43%, but partially quenched by 12% when exposed to propane gas in dry nitrogen. Thus this system can differentiate between alkanes and alkenes. The enhancement in fluorescence intensity upon exposure to propylene was proposed to be due to the formation of a π–cation interaction between an alkene analyte and the Ag^+ cation thus weakening the π–cation interaction between the Ag^+ cation and the bpee ligand. The sensing response to propylene was reversible, but heating at 60 °C under vacuum followed by nitrogen purging was required. The response to 1-hexene was also tested. Upon exposure to 1-hexene vapour a fluorescence intensity enhancement of ∼43% was measured which suggests that differentiation between different alkenes may not be possible with this MOF system.

Furukawa *et al.* investigated how the crystal orientation of a MOF impacted on its adsorption kinetics.[171] The MOF used was [Zn(NO$_2$-ip)(4,4′-bipy)] (NO$_2$-ip = 5-nitroisophthalate), Zn-CID-5, and thin films of the MOF were grown solvothermally on QCM sensors, one of which had been modified with 16-mercapto-hexadecanoic acid and the other remained bare. The presence of 16-mercaptohexadecanoic acid on the surface of the QCM favoured the orientation of the Zn-CID-5 crystals in the [1−1−1] direction whereas the preferred crystal direction of the Zn-CID-5 crystals on the bare QCM sensor was [100]. Zn-CID-5 crystals were also solvothermally grown on the surface of a bare QCM sensor in the presence of 4-phenylpyridine, which is a crystal size modulator. This led to a preferred orientation of the Zn-CID-5 crystals along the [010] direction. From adsorption kinetic studies it was found that Zn-CID-5 orientated along the [010] direction had the fastest adsorption kinetics and thus was the most suitable for sensing. The sensor showed the largest sensing responses to methanol compared to hexane as the methanol induced a 'gate-opening' phenomenon whereas hexane did to a far lesser extent. The sensing response to methanol was reversible, but the time response was over 100 s.

Finally Cao *et al.* reported a colorimetric detector for methanol vapour that was comprised of a solvothermally grown film of the MOF [Co$_3$(tbtc)$_2$(DMF)$_2$]·4DMF (tbtc = 4-[[3,5-bis[(4-carboxylato-phenoxy)methyl]-2,4,6-trimethyl-phenyl]methoxy]benzoate, Fig. 17) on an alumina support.[172] Upon exposure to air saturated with methanol vapour the colour of the thin film changed from blue to pink over several hours of exposure. However, the colour could only be restored by exposing the MOF thin film to DMF vapour.

3.6 Ammonia sensors

3.6.1 Zeolites for sensing NH$_3$. The detection of residual ammonia in the exhaust stream of diesel engines is necessary for efficient use of selective catalytic reduction (SCR) catalysts. Many zeolite-based ammonia sensing techniques exploit the proton conductive properties of zeolites. The earliest example reported the effect of NH$_3$ (up to 25 ppm concentration) on the electrical properties of the Na$^+$- and H$^+$-forms of beta polymorph A-type zeolites using impedance spectroscopy.[96] In the presence
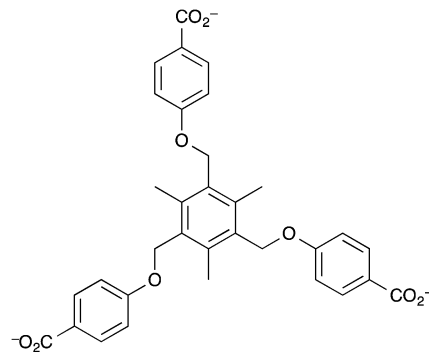

Fig. 17 The 4-[[3,5-bis[(4-carboxylatophenoxy)methyl]-2,4,6-trimethyl-phenyl]methoxy]benzoate (tbtc) ligand.[172]

of ammonia the ionic conductivity of Na-beta polymorph A is unaffected, while it promotes proton conduction in H-beta polymorph A, opening the way to conductive proton zeolite sensing. Other zeolite types have also been found to be efficient proton conductive materials.

Pt-doped zeolite Y assembled in films was promising, but showed a strong cross-sensitivity to NO.[92] In contrast, the zeolite H-ZSM-5 had very small cross sensitivity to NO, CO, CO$_2$ and hydrocarbons as no metal elements were incorporated in the zeolite structure. It provided a response time of seconds and a detection limit down to 5 ppm concentration of ammonia in synthetic air.[85] To improve the sensitivity of a Fe-doped poly(*p*-phenylene) polymer (Fe-dPPP) sensor towards NH$_3$, several forms of ZSM-5 zeolites (Na$^+$, K$^+$, NH$_4^+$, H$^+$) were added into the conductive polymer matrix.[86] The highest electrical conductivity sensitivity was obtained with the composite Fe-dPPP–H-ZSM-5. This was explained by the high acidity, pore volume and surface area of the H-form of ZSM-5 zeolite, as those properties favour both conductive polymer interaction and NH$_3$ adsorption. In addition, the FTIR spectrum showed that the NH$_3$–polymer interaction is irreversible while the NH$_3$–zeolite interaction is reversible. The irreversibility of the NH$_3$–polymer interaction was recently resolved by the same research group. Indeed, they reported that a composite comprised of HClO$_4$-doped poly(3-thiopheneacetic acid) as polymer and a zeolite Y gave similar results with a fully reversible NH$_3$–polymer interaction.[122]

The interaction of ammonia with Ag$^+$-exchanged zeolite Y was recently exploited to demonstrate potential for NH$_3$ detection.[123] As no measurable self-reduction of Ag$^+$, and therefore, no proton-mediated change of impedance could be recorded in the presence of NH$_3$, the impedance measurements were based directly on the mobility change of the Ag$^+$ in the presence of NH$_3$. No cross-sensitivity was observed for O$_2$, CO, CO$_2$ and propane, though there was some interference from NO and water.

Sensors for ammonia based on non-proton conductive zeolite properties have also been developed. An H-ZSM-5 zeolite thin film was grown on a long-period fibre grating whereupon the adsorption-induced shift of the resonant wavelength of the fibre grating was monitored during exposure to ammonia.[87] This sensor had a 2 min response time for adsorption–desorption of NH$_3$ in 612 ppmv ammonia in nitrogen atmosphere. Recently, a

This journal is © The Royal Society of Chemistry 2015

Chem. Soc. Rev., 2015, **44**, 4290–4321 | 4313

sensor based on the conductivity of metal oxide was reported. Indeed, semiconducting zinc oxide covered with zeolite (Y, mordenite or beta polymorph A) showed sensitivity down to a few ppm concentration of NH₃.[49]

Another gas detector containing a protective layer of a zeolite with a thickness of approximately 10 μm was applied as ammonia sensor in the control loop of a NO$_x$ storage catalyst for diesel engines.[51] It was reported that ammonia could be detected in oxygen-rich gases containing nitrogen oxides such as exhaust gases or flue gases, using a condenser based on a hydrophobic, noble metal-free zeolite of low acidity having an ordered crystalline structure such as zeolite Y, mordenite or ZSM-5.[52]

3.6.2 MOFs for sensing NH₃. The floating gate field effect transistor (FGFET) gas sensor consisting of a gold electrode modified with HKUST-1, developed by Fleischer *et al.* and described in Section 3.1.2, also demonstrated sensitivity to 5 ppm of ammonia.[146] The authors reasoned that the small kinetic diameter of ammonia allowed for it to pass through the pores of the HKUST-1 overlayer and interact with the gold electrode, thus causing a measurable change in work function. However, the magnitude of the change in the work function was similar to that measured upon exposure to 3 ppm of hydrogen sulfide.

Humphrey *et al.* have developed the PCM-15 MOF previously reported as a detector material for humidity (Section 3.1.2) for the detection of other gases and vapours.[134,135] In particular, ammonia was found to be a more efficient quencher of the luminescence of the terbium(III) ion than water. Upon activation of the MOF at 150 °C under vacuum for 1 h, the intensity of the photoluminescence due to the terbium ion was found to double. Then upon treatment with 1 atm of ammonia gas, the photoluminescence intensity decreased 1.4 times relative to the photoluminescence intensity measured when the MOF was exposed to water vapour. PCM-15 exhibited selectivity to ammonia over hydrogen when exposed to low concentrations of ammonia gas in hydrogen carrier gas. This shows promise in detection of low concentrations of impurity gases or vapours in feedstock gases, but the major disadvantage with this system is that the detection of ammonia is irreversible.

Dincă *et al.* reported two MOFs that function as selective detectors for ammonia at 100 °C, but not at room temperature.[173] [Zn₂(tpce)] (tpce = tetrakis(phenylcarboxylate)ethylene, Fig. 18) and [Mg₂(dobdc)] (dobdc = 2,5-dioxobenzene-1,4-dicarboxylate, Fig. 18), both displayed fluorescence "turn-on" upon exposure to ammonia as opposed to the typical fluorescence "turn-off" mechanism, otherwise known as quenching. Fluorescence "turn-on" describes the interaction between an analyte and a "dark" fluorophore resulting in the "switch on" of the "dark" species so that it luminesces. In addition the maximum emission wavelengths of both MOFs shifted upon interaction with ammonia at 100 °C. [Zn₂(tpce)] exhibited a emission wavelength redshift from 487 nm to 511 nm when exposed to ammonia at 100 °C. In addition [Zn₂(tpce)] was thermally stable up to ~400 °C. Exposure to ammonia led to an irreversible phase change in [Zn₂(tpce)] to an unidentified crystalline form, so the detection of ammonia is irreversible. However, [Mg₂(dobdc)], in which Mg²⁺ ions are coordinated by dobdc ions, exhibited a
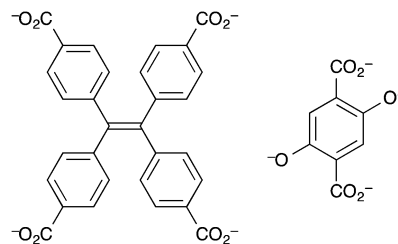

Fig. 18 The tetrakis(phenylcarboxylate)ethylene (tpce) ligand (left) and 2,5-dioxobenzene-1,4-dicarboxylate (dobdc) ligand (right) in the MOFs reported by Dinč *et al.* for detection of ammonia.[173]

reversible "turn-on" fluorescence response upon exposure to ammonia at 100 °C, after activation at 180 °C for 12 h. This MOF also exhibited selectivity over methanol and ethanol and was thermally stable up to ~250 °C.

3.7 Hydrogen sulfide sensors

3.7.1 MOFs for sensing H₂S. While there have been no reports of zeolites for sensing H₂S in the literature, there have been reports of MOF materials having sensitivity for H₂S. For example, Lu *et al.* reported a nanoparticulate copper(I) MOF, with a ligand based on 3-amino-1,2,4-triazole-5-thiol (Fig. 19), that exhibited a decrease in fluorescence intensity and a visible colour change upon exposure to hydrogen sulfide gas.[174]

The material demonstrated a remarkable fluorescence Stokes shift of large magnitude upon excitation at 365 nm when dispersed in DMF. The resulting red fluorescence emission, λ_{max} = 620 nm, was quenched by as little as 2 ppm of H₂S in nitrogen carrier gas, but not by other gases or vapours such as CO₂, ethanol or even air. In addition an accompanying colour change from yellow to brown could also act as an indicator of hydrogen sulfide exposure. The proposed mechanism for fluorescence quenching involves a reaction between the MOF and H₂S to form a copper sulfide, Cu₉S₈ suggesting that the detection mechanism is irreversible.

The FGFET gas sensor modified with HKUST-1 reported by Fleischer *et al.*, and described in Section 3.1.2, also demonstrated sensitivity to 3 ppm of hydrogen sulfide.[146] The authors reasoned that the small kinetic diameter of hydrogen sulfide allowed for it to pass through the pores of the HKUST-1 overlayer and interact with the gold electrode. However, the magnitude of the change in the work function was similar to 5 ppm of ammonia.

3.8 Sulfur dioxide sensors

3.8.1 Zeolites for sensing SO₂. Sulfur dioxide contributes to acid rain and decreased air quality and is subject to legislated emissions limits. The sensors currently used for controlling the
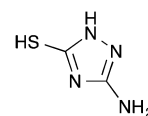

Fig. 19 The 3-amino-1,2,4-triazole-5-thiol ligand used by Lu *et al.* to synthesise MOF nanoparticles which were fluorescently quenched in the presence of hydrogen sulfide gas.[174]

4314 | *Chem. Soc. Rev.*, 2015, **44**, 4290–4321

This journal is © The Royal Society of Chemistry 2015

combustion process in track, car and jet engines suffer from poisoning by sulfur oxides. A gas-absorbing layer for trapping SO_2 prior to sensing the other gases at high-temperature is still a challenging assignment.

The history of sulfur dioxide removal from gas streams by using zeolite adsorbents is lengthy. A comparative study including natural and synthetic zeolites revealed that the SO_2 capacity of the latter is higher, which is due to higher purity and the controlled characteristics of the synthetic materials.[200] In the 1970s, synthetic mordenite- and faujasite (FAU)-type zeolites were employed for SO_2 adsorption because of their stability under acidic conditions. A general understanding is that the sulfur dioxide is adsorbed by hydrogen bonding to one or two conveniently positioned surface hydroxyl groups of the zeolites. It was found that the stronger the acidity, the higher the electron deficiency, the better the sulfur resistance. It was also found that the adsorption of sulfur on Pd-containing FAU zeolite is reversible.[124,125] The investigation of SO_2 adsorption on silicalite-1 and de-aluminated zeolite Y showed the supremacy of all-silica pentasil-type molecular sieve towards SO_2.

Faujasite-type zeolites were reported to be useful for sensing SO_2 when combined with metal species. In a first example, a layer of faujasite-type zeolite deposited on QCM oscillators, with an electrode of gold, is active as the increased mass due to absorbed SO_2 reduces the frequency of the QCM.[101] In further work zeolite A, was deposited on the QCM. The zeolite-A doped QCM could monitor 50 ppm of SO_2 in He at 170 °C.[57]

More recently, the effect of various transition metal cations (Mn^{2+}, Fe^{2+}, Co^{2+}, Ni^{2+}, Cu^{2+} and Zn^{2+}) exchanged into hydrated Y-type zeolites for SO_2 sensing were investigated by electrical conductivity.[126] When exposed to a SO_2 atmosphere, all poly(3,4-ethylenedioxythiophene)–poly(styrene sulfonic acid)/metal doped zeolite Y composites, and especially the Mn^{2+} doped zeolite, showed higher sensitivity than a pristine conductive polymer matrix used as reference though at the expense of longer response times. The authors attributed those results to the electronegativity of the metal cations which strongly improved the adsorption properties of the zeolite Y, and hence the electrical sensitivity of the composite.

Often sensing of different gases by zeolite molecular sieves faces problems due to catalytic side reactions. For instance, the sodium form of zeolite Y demonstrated impressive adsorptive and catalytic properties in NO_x elimination from exhaust gases of diesel and lean burn engines. Physisorbed SO_2, HSO_3^- and $S_2O_5^{2-}$ species in the Na–Y adsorbent were observed, and the poisoning of N_2O_3 adsorption sites by SO_2 was found to be a function of sodium hydrogen sulfite formed in the channels. A possibility of overcoming the poisoning of the N_2O_3 adsorption capacity of Na–Y zeolite by SO_2 was based on short adsorption–desorption cycles, high temperature and low oxygen concentrations during the desorption process. Sultana et al.[127] studied the adsorptive separation of NO_x in the presence of SO_x on Na-Y zeolite. They found that when Na-Y zeolite operates in a pressure swing process for NO_x removal from engine exhausts, it is fairly resistant to SO_2. However, poisoning by SO_2 could be suppressed by using short adsorption–desorption cycles, by limiting the

oxygen concentration in the regeneration gas and by working at temperatures higher than 255 °C.

The elimination of SO_2 by microporous zeolite-type materials is based on either low or high silica zeolites. The SO_2 molecule reacts with the metals situated in the pores of the zeolite structure leading to metal sulfate formation. This leads to channel blocking and a substantial decrease of transport is observed. Another disadvantage of low silica zeolite materials is their hydrophilic nature. Thus, the gas adsorption capacity is dramatically reduced by concurrent water adsorption. Furthermore, low-silica zeolites are not adapted for SO_2 retention since their chemical stability in acidic media is limited. The increase of silicon content in zeolites leads to a decrease of their hydrophilicity, which can reach a level when the water molecules are rejected by the microporous structure. Such types of zeolitic materials are often employed in selective adsorption of SO_2 and other sulfur compounds. The main advantage of these materials is their higher stability than other absorbers towards SO_2 and possible regeneration for multiple usages due to their high thermal stability (900 °C) and high stability in an acidic media. In summary, the high silica zeolite films will allow discrimination of H_2O molecules and selective adsorption of SO_2. The latter is particularly important to retain the high capacity of the zeolite sorbent. SO_2 detection on high silica zeolites is essentially unaffected by the presence of CO_2 and other gases.

No examples of the use of MOFs for SO_2 sensing were found in the literature. However, it should be noted that sulfur dioxide (SO_2) adsorption in MOFs has been reported,[201–205] thus MOFs that possess suitable stability for automotive exhaust gas sensing hold promise as potential sensing materials for SO_2.

3.9 Hydrogen sensors

3.9.1 Zeolites for sensing of H_2. Metal oxides impregnated into zeolite pores have been used to achieve sensitive H_2 sensing. One example sensor by Wark et al. was described in Section 3.4.1 as a CO sensor. The detector consisted of titanium dioxide clusters immobilised in the pores of zeolite NaY and it showed similar stability and response times towards H_2 as it did to CO.[114] Other reports described the use of tin oxide impregnated on the external surface of zeolite Y.[206,207] The composite material obtained showed a linear resistance response to the adsorption of H_2.

Silicalite zeolite can also be used as a filter. As described for humidity sensors, Santamaria et al. showed that the silicalite coating on SnO_2 gave enhanced response to both H_2O and H_2.[58] Recently, a fibre optic sensor consisting of a proton-conducting $SrCe_{0.8}Zr_{0.1}Y_{0.1}O_{2.95}$ thin film overcoated by silicalite zeolite layer was reported.[93] Pores of the zeolitic filter were found to be small enough to permit H_2 diffusion but restricted the diffusion of other gases and fine particles from dusty coal or biomass gasification processes. When the silicalite film was less than 2.5 μm thick, a high sensitivity of 0.14 nm kPa^{-1}-H_2 was observed.

3.9.2 MOFs for sensing of H_2. As described above, there are two uses of MOFs in gas sensors; as a functional active sensing element or as an auxiliary element. For sensing gaseous hydrogen, H_2, MOFs have been used as auxiliary filter layer elements, enhancing the selectivity of the sensor device to hydrogen.

Hupp *et al.* developed an optical sensor device that utilised Bragg grating stacks made from subsequential layers of ZIF-8 and palladium. A Bragg grating stack operates as a wavelength-selective mirror; some wavelengths are reflected whereas other wavelengths are transmitted. The wavelength reflected depends on the refractive index of the materials in the Bragg stack. If the refractive index of some of the layers within the Bragg grating stack changes then the wavelengths that are reflected also change. Hupp *et al.*'s Bragg grating stack comprised of two sets of a bilayer structure of Pd ($\sim$10 nm)/ZIF-8 ($\sim$300 nm) that operate at visible-light wavelengths, and the authors predicted, that upon exposure to certain analyte gases, the refractive index of the ZIF-8 layers would change due to adsorption of the analyte gases.[162] Upon exposure to vapours of short chain length alkanes, which all have kinetic diameters >4 Å,[208] the refractive index of the ZIF-8 layers increased due to adsorption of these compounds. However, the sensor device did not offer differentiation between the alkane analytes. In contrast, when the sensor was exposed to increasing concentrations of H_2 in N_2 carrier gas, from 0% up to 5%, the wavelengths reflected did not change but the transmission intensity increased. The authors therefore postulated that the H_2 was insignificantly adsorbed within or on the ZIF-8 layers so as not to change the refractive index of the Bragg grating stack, but was reversibly adsorbed onto the palladium layer and forming a palladium hydride that is more transparent in the visible wavelengths than the $\sim$10 nm thick palladium layer. Therefore, by measuring the transmission intensity of the device during exposure to analytes, it was observed that the device possessed a selective affinity for hydrogen gas molecules over short alkyl chain vapour molecules which is due to difference in kinetic diameters; the kinetic diameter of H_2 is 2.89 Å and the pore window size of ZIF-8 is 3.40 Å.[209] Therefore the ZIF-8 layers acted as size selective filter layers. Sensing experiments with carbon dioxide, CO_2, which has a kinetic diameter of 3.30 Å[210] further confirmed that ZIF-8 acted as a size selective filter layer. Upon exposure to CO_2 an increase in transmission intensity was measured; carbon dioxide is smaller than the pore size window of ZIF-8 and thus passes through the ZIF-8 pores and interacts with the palladium layer.

Dam *et al.* also utilised a MOF layer as a filter to achieve selective optical detection of hydrogen gas.[147] The authors chose a copper btc material as the gas selective filter layer as this had been shown to possess increased selectivity towards H_2 when in a thin film. Dam *et al.* deposited the MOF thin film through a layer-by-layer deposition process onto a palladium substrate that had been initially covered with a self-assembled monolayer of glycine. With this technique, the MOF thin film was found to be mostly amorphous though the authors argued that the chemical environment within this film was similar to that within HKUST-1 based on FTIR spectral data. The resulting sensor was interrogated with optical transmission spectroscopy whilst exposed to a H_2 environment. Increases in the optical transmission were measured upon exposure to hydrogen gas at various concentrations at room temperature and 100 °C, but concentration differentiation was greatest when measurements

were taken at 100 °C. The device showed stable repeatable and reversible responses, but the response time was on the order of 1000 s. Selectivity to hydrogen gas over O_2, CO_2 and CH_4 in gas mixtures was demonstrated, but the kinetics of adsorption of hydrogen were significantly decreased when the device was exposed to H_2–CO and H_2–H_2O mixtures. This could be due to the affinity of the copper MOF for H_2O and CO; these gases preferentially adsorb and thus hinder the ingress of H_2.[211,212]

4. Conclusions and future perspectives

It is clear that porous materials, exemplified by zeolites and MOFs, offer tremendous flexibility and versatility in terms of selectivity and sensitivity and thus demonstrate great promise for the fabrication of sensors for exhaust gases and vapours. Both size and shape selectivity have been demonstrated with zeolite- and MOF-based detectors *via* control of the dimensions of the pores, and in some cases the crystal orientation when in ordered films, thus enabling detection and differentiation between gases and vapours. Chemical selectivity and sensitivity have been controlled by the incorporation of select dopants into the frameworks so as to elicit desirable optical and or electrochemical responses upon interaction with analytes.

In this review, we summarised 170 different published sensors including around a third based on MOFs and two-thirds based on zeolites (Fig. 20). Among those publications, hydrocarbon sensors are currently the most common for both zeolites and MOFs. Zeolite and MOF sensors were developed in similar numbers for automotive exhaust vapours, though no NOx and SO_2 sensors based on MOFs were reported whereas only MOF-based sensors have been reported to detect H_2S.

The greater chemical and thermal stability of zeolites, coupled with the ability to be more easily integrated into smaller electrical
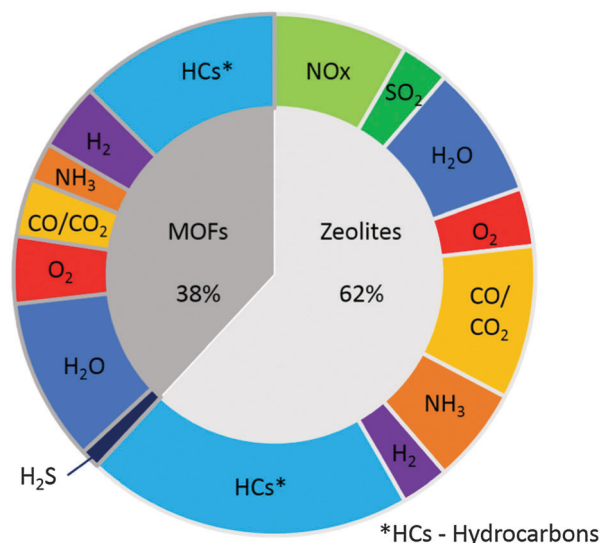

Fig. 20 Reported sensors based on zeolites or MOFs along with the type of sensors.

sensors, means zeolites may be the most suitable sensing materials for use in prospective on-board exhaust gas sensors. The lower chemical and thermal stability of MOFs suggests that these materials are more suited to fabricate sensors for exhaust gas emissions during commissioning of new vehicles in production; location in a production setting will allow for appropriate gas cooling and clean-up before sensing which would be impractical on-board vehicles.

The wide variety of organic linkers and metal nodes that can be incorporated into MOFs has allowed for increased sensitivity and selectivity based on control of the interactions between adsorbed analytes. Finally, it needs to be acknowledged that the field of MOFs for sensing is young in comparison to the research into the use of zeolites as sensor materials. While in most cases at the current time, zeolite-based sensors are more advanced than MOF-based analogues, it is expected that advances in discriminatory sensing, sensitivity and thermal stability will enable this gap to be closed in the future.

Despite their promise, few of these systems have to date been incorporated into devices that allow for real-time and on-line data collection and thus most only exist as detectors or probes under specific conditions. In addition, few examples of these materials have been shown to exhibit successful sensing of specific species when exposed to varying temperatures, pressures and in the presence of contaminants.

The sensitivity and selectivity that can be explicitly controlled by sensor designers when using MOFs and zeolites and the great need economically and environmentally for energy efficient transport indicates that the development of porous materials for automotive gas sensing will continue to be an active research field in the future.

Acknowledgements

References

1 M. A. Liberman, *Introduction to Physics and Chemistry of Combustion: Explosion, Flame, Detonation*, Springer, Berlin Heidelberg, 2008.

2 United Nations, Kyoto Protocol to the United Nations Framework Convention on Climate Change, 1998.

3 United States Environmental Protection Agency, U.S. Greenhouse Gas Inventory Report, 2014.

4 S. E. Manahan, *Fundamentals of Environmental Chemistry*, CRC Press, 2nd edn, 2000.

5 International Energy Agency (IEA), Key World Energy Statistics 2014, 2014.

6 Institution of Mechanical Engineers, Low Carbon Vehicles: Driving the UK's Transport Revolution, 2010.

7 Department for Business, Enterprise and Regulatory Reform, An Independent Report on the Future of the Automotive Industry in the UK, 2009.

8 N. Jackson, Technology Roadmap, the R&D Agenda and UK Capabilities, Automotive Council UK, 2010.

9 L. Chapman, *J. Transp. Geogr.*, 2007, **15**, 354.

10 The European Parliament and Council of the European Union, Off. J. Eur. Union, 52, 1., 2009.

11 A. M. K. P. Taylor, *Energy Policy*, 2008, **36**, 4657.

12 D. Carslaw, S. Beevers, E. Westmoreland, M. Williams, J. Tate, T. Murrells, J. Stedman, Y. Li, S. Grice, A. Kent and I. Tsagatakis, Trends in NO_x and NO_2 Emissions and Ambient Measurements in the UK, DEFRA, 2011.

13 P. Mock, J. German, A. Bandivadekar, I. Riemersma, N. Ligterink and U. Lambrecht, From Laboratory to Road: A Comparison of Official and 'Real-World' Fuel Consumption and CO_2 Values for Cars in Europe and the United States, The International Council on Clean Transportation, 2013.

14 M. Tutuianu, A. Marotta, H. Steven, E. Ericsson, T. Haniu, N. Ichikawa and H. Ishii, in 68th Session of Working Party on Pollution and Energy, United Nations Economic Commission for Europe, 2013, 98.

15 *Diesel Engine Management: Systems and Components*, ed. K. Reif, Springer Vieweg, Wiesbaden, 2014.

16 M. J. Nunney, *Light and Heavy Vehicle Technology*, Routledge, 4th edn, 2006.

17 N. Docquier and S. Candel, *Prog. Energy Combust. Sci.*, 2002, **28**, 107.

18 J. Riegel, H. Neumann and H.-M. Wiedenmann, *Solid State Ionics*, 2002, **152–153**, 783.

19 U. Kiencke and L. Nielsen, *Automotive Control Systems: For Engine, Driveline, and Vehicle*, Springer-Verlag, Berlin, 2nd edn, 2005.

20 T. Wagner, S. Haffer, C. Weinberger, D. Klaus and M. Tiemann, *Chem. Soc. Rev.*, 2013, **42**, 4036.

21 E. Llobet, *Sens. Actuators, B*, 2013, **179**, 32.

22 S. Ozdemir and J. Gole, *Curr. Opin. Solid State Mater. Sci.*, 2007, **11**, 92.

23 E. L. First, C. E. Gounaris and C. A. Floudas, *Langmuir*, 2013, **29**, 5599.

24 R. Matsuda, *Nature*, 2014, **509**, 434.

25 Y. Zheng, X. Li and P. K. Dutta, *Sensors*, 2012, **12**, 5170.

26 X. Xu, J. Wang and Y. Long, *Sensors*, 2006, **6**, 1751.

27 X. Wan, H. Song, D. Zhao, L. Zhang and Y. Lv, *Sens. Actuators, B*, 2014, **201**, 413.

28 J. Lei, R. Qian, P. Ling, L. Cui and H. Ju, *TrAC, Trends Anal. Chem.*, 2014, **58**, 71.

29 K. S. Park, Z. Ni, A. P. Côté, J. Y. Choi, R. Huang, F. J. Uribe-Romo, H. K. Chae, M. O'Keeffe and O. M. Yaghi, *Proc. Natl. Acad. Sci. U. S. A.*, 2006, **103**, 10186.

30 H. O. Pastore, E. C. Oliveira, A. Frache, S. R. Dutra, E. Boccaleri and L. Marchese, in *Studies in Surface Science and Catalysis*, ed. E. van Steen, M. Claeys and L. H. Callanan, Elsevier, 2004, vol. 154B, p. 1426.

31 Y. Cui, Y. Yue, G. Qian and B. Chen, *Chem. Rev.*, 2012, **112**, 1126.

32 L. E. Kreno, K. Leong, O. K. Farha, M. Allendorf, R. P. Van Duyne and J. T. Hupp, *Chem. Rev.*, 2012, **112**, 1105.

33 A. Bétard and R. A. Fischer, *Chem. Rev.*, 2012, **112**, 1055.

34 O. Shekhah, J. Liu, R. A. Fischer and C. Wöll, *Chem. Soc. Rev.*, 2011, **40**, 1081.

35 K. J. Mohan, K. Jagadeesan and A. Yadav, *IOSR J. Environ. Sci., Toxicol. Food Technol.*, 2013, **6**, 1.

36 D. Banerjee, Z. Hu and J. Li, *Dalton Trans.*, 2014, **43**, 10668.

37 S. M. Auerbach, K. A. Carrado and P. K. Dutta, *Handbook of Zeolite Science and Technology*, CRC Press, 2003.

38 *Ordered Porous Solids: Recent Advances and Prospects*, ed. V. Valtchev, S. Mintova and M. Tsapatsis, Elsevier, 2008.

39 M. Zaarour, B. Dong, I. Naydenova, R. Retoux and S. Mintova, *Microporous Mesoporous Mater.*, 2014, **189**, 11.

40 *Post-Synthesis Modification I*, ed. H. G. Karge and J. Weitkamp, Springer, Berlin Heidelberg, 2002.

41 *Introduction to Zeolite Molecular Sieves*, ed. J. Cejka, H. van Bekkum, A. Corma and F. Schueth, Elsevier, 3rd edn, 2007.

42 S. Babel and T. A. Kurniawan, *J. Hazard. Mater.*, 2003, **97**, 219.

43 M. M. Scherer, S. Richter, R. L. Valentine and P. J. J. Alvarez, *Crit. Rev. Environ. Sci. Technol.*, 2000, **30**, 363.

44 S. Mintova and E.-P. Ng, in *Comprehensive Inorganic Chemistry II*, ed. J. Reedijk and K. Poeppelmeier, Elsevier, 2013, vol. 5, p. 285.

45 J.-P. Gilson, O. Marie, S. Mintova and V. Valtchev, *Emerging Applications of Zeolites*, 3rd FEZA School on Zeolites, Valencia, Spain, 2011, p. 245.

46 K. Fukui and S. Nishida, *Sens. Actuators, B*, 1997, **45**, 101.

47 S. Sohrabnezhad, A. Pourahmad and M. A. Sadjadi, *Mater. Lett.*, 2007, **61**, 2311.

48 M. A. Zanjanchi and S. Sohrabnezhad, *Sens. Actuators, B*, 2005, **105**, 502.

49 D. C. Pugh, E. J. Newton, A. J. T. Naik, S. M. V. Hailes and I. P. Parkin, *J. Mater. Chem. A*, 2014, **2**, 4758.

50 I. Yimlamai, S. Niamlang, P. Chanthaanont, R. Kunanuraksapong, S. Changkhamchom and A. Sirivat, *Ionics*, 2011, **17**, 607.

51 E. Irion, A. Knezevic, H. Leye and M. Smuk, *DE Pat.*, DE10133997, 2003.

52 U. Flesch, A. Kayser, W. Maunz, R. Moos, R. Muller, C. Plog, W. Schäfer and U. Simon, *EP Pat.*, EP0871031A3, 1998.

53 M. Vilaseca, J. Coronas, A. Cirera, A. Cornet, J. R. Morante and J. Santamaria, *Sens. Actuators, B*, 2008, **133**, 435.

54 M. A. Urbiztondo, A. Peralta, I. Pellejero, J. Sesé, M. P. Pina, I. Dufour and J. Santamaria, *Sens. Actuators, B*, 2012, **171–172**, 822.

55 S. Mintova and T. Bein, *Microporous Mesoporous Mater.*, 2001, **50**, 159.

56 S. Mintova, S. Mo and T. Bein, *Chem. Mater.*, 2001, **13**, 901.

57 I. Sasaki, H. Tsuchiya, M. Nishioka, M. Sadakata and T. Okubo, *Sens. Actuators, B*, 2002, **86**, 26.

58 M. Urbiztondo, I. Pellejero, A. Rodriguez, M. P. Pina and J. Santamaria, *Sens. Actuators, B*, 2011, **157**, 450.

59 M. Vilaseca, J. Coronas, A. Cirera, A. Cornet, J. R. Morante and J. Santamaria, *Sens. Actuators, B*, 2007, **124**, 99.

60 A. Afonja, S. Dungey, R. Binions, I. Parkin, D. Lewis and D. Williams, *ECS Trans.*, 2009, **16**, 77.

61 R. Binions, H. Davies, A. Afonja, S. Dungey, D. Lewis, D. E. Williams and I. P. Parkin, *J. Electrochem. Soc.*, 2009, **156**, J46.

62 N. Densakulprasert, L. Wannatong, D. Chotpattananont, P. Hiamtup, A. Sirivat and J. Schwank, *Mater. Sci. Eng., B*, 2005, **117**, 276.

63 K. E. Yasuda, J. H. Visser and T. Bein, *Microporous Mesoporous Mater.*, 2009, **119**, 356.

64 R. Binions, A. Afonja, S. Dungey, D. W. Lewis, I. P. Parkin and D. E. Williams, *IEEE Sens. J.*, 2011, **11**, 1145.

65 L. Wannatong and A. Sirivat, *React. Funct. Polym.*, 2008, **68**, 1646.

66 T. Baimpos, L. Gora, V. Nikolakis and D. Kouzoudis, *Sens. Actuators, A*, 2012, **186**, 21.

67 A. Zampieri, A. Dubbe, W. Schwieger, A. Avhale and R. Moos, *Microporous Mesoporous Mater.*, 2008, **111**, 530.

68 R. Bruck and K. Althoefer, *DE Pat.*, DE102004053460, 2006.

69 C. Chuapradit, L. R. Wannatong, D. Chotpattananont, P. Hiamtup, A. Sirivat and J. Schwank, *Polymer*, 2005, **46**, 947.

70 M. Vilaseca, J. Coronas, A. Cirera, A. Cornet, J. R. Morante and J. Santamaría, *Catal. Today*, 2003, **82**, 179.

71 L. Scandella, G. Binder, T. Mezzacasa, J. Gobrecht, R. Berger, H. P. Lang, C. Gerber, J. K. Gimzewski, J. H. Koegler and J. C. Jansen, *Microporous Mesoporous Mater.*, 1998, **21**, 403.

72 P. Sazama, H. Jirglová and J. Dědeček, *Mater. Lett.*, 2008, **62**, 4239.

73 S. Neumeier, T. Echterhof, R. Bölling, H. Pfeifer and U. Simon, *Sens. Actuators, B*, 2008, **134**, 171.

74 A. Satsuma, D. Yang and K. Shimizu, *Microporous Mesoporous Mater.*, 2011, **141**, 20.

75 P. Chanthaanont and A. Sirivat, *e-Polym.*, 2012, **12**, 106.

76 L. Gora, J. Kuhn, T. Baimpos, V. Nikolakis, F. Kapteijn and E. M. Serwicka, *Analyst*, 2009, **134**, 2118.

77 A. Dubbe, *Sens. Actuators, B*, 2009, **137**, 205.

78 G. Hagen, A. Dubbe, G. Fischerauer and R. Moos, *Sens. Actuators, B*, 2006, **118**, 73.

79 S. Reiß, G. Hagen and R. Moos, *Sensors*, 2008, **8**, 7904.

80 A. Dubbe and R. Moos, *Electrochem. Solid-State Lett.*, 2006, **9**, H31.

81 A. Dubbe, *Solid State Ionics*, 2008, **179**, 1645.

82 A. Dubbe and R. Moos, *Sens. Actuators, B*, 2008, **130**, 546.

83 K. Sahner, D. Schönauer, R. Moos, M. Matam and M. L. Post, *J. Mater. Sci.*, 2006, **41**, 5828.

84 K. Sahner, R. Moos, M. Matam, J. J. Tunney and M. Post, *Sens. Actuators, B*, 2005, **108**, 102.

85 M. E. Franke, U. Simon, R. Moos, A. Knezevic, R. Müller and C. Plog, *Phys. Chem. Chem. Phys.*, 2003, **5**, 5195.

86 P. Phumman, S. Niamlang and A. Sirivat, *Sensors*, 2009, **9**, 8031.

87 X. Tang, Z. Tang, S. J. Kim and J. Dong, *Proc. SPIE*, 2009, **7293**, 72931E.

88 G. Hagen, I. Marr and R. Moos, *Sens. Lett.*, 2011, **9**, 902.

4318 | *Chem. Soc. Rev.*, 2015, **44**, 4290–4321

This journal is © The Royal Society of Chemistry 2015

89 D. Jadsadapattarakul, C. Thanachayanont, J. Nukeaw and T. Sooknoi, *Sens. Actuators, B*, 2010, **144**, 73.

90 M. Grahn, Z. Wang, M. Lidström-Larsson, A. Holmgren, J. Hedlund and J. Sterte, *Microporous Mesoporous Mater.*, 2005, **81**, 357.

91 J. Zhang, X. Tang, J. Dong, T. Wei and H. Xiao, *Sens. Actuators, B*, 2009, **135**, 420.

92 R. Moos, R. Müller, C. Plog, A. Knezevic, H. Leye, E. Irion, T. Braun, K.-J. Marquardt and K. Binder, *Sens. Actuators, B*, 2002, **83**, 181.

93 H. Jiang, R. Yang, X. Tang, A. Burnett, X. Lan, H. Xiao and J. Dong, *Sens. Actuators, B*, 2013, **177**, 205.

94 S. Thomas, P. Bazin, L. Lakiss, V. de Waele and S. Mintova, *Langmuir*, 2011, **27**, 14689.

95 L. Lakiss, S. Thomas, P. Bazin, V. de Waele and S. Mintova, *Microporous Mesoporous Mater.*, 2014, **200**, 326.

96 U. Simon, U. Flesch, W. Maunz, R. Müller and C. Plog, *Microporous Mesoporous Mater.*, 1998, **21**, 111.

97 P. Payra and P. K. Dutta, *Microporous Mesoporous Mater.*, 2003, **64**, 109.

98 M. A. Coutant, P. Payra and P. K. Dutta, *Microporous Mesoporous Mater.*, 2003, **60**, 79.

99 K. L. McGilvray, M. N. Chrétien, M. Lukeman and J. C. Scaiano, *Chem. Commun.*, 2006, 4401.

100 C. Plog, W. Maunz, P. Kurzweil, E. Obermeier and C. Scheibe, *Sens. Actuators, B*, 1995, **25**, 403.

101 M. Osada, I. Sasaki, M. Nishioka, M. Sadakata and T. Okubo, *Microporous Mesoporous Mater.*, 1998, **23**, 287.

102 I. Pellejero, M. Urbiztondo, D. Izquierdo, S. Irusta, I. Salinas and M. P. Pina, *Ind. Eng. Chem. Res.*, 2007, **46**, 2335.

103 N. Li, X. Li, T. Zhang, S. Qiu, G. Zhu, W. Zheng and W. Yu, *Mater. Lett.*, 2004, **58**, 1535.

104 T. A. Ruda-Eberenz, A. Nagy, W. J. Waldman and P. K. Dutta, *Langmuir*, 2008, **24**, 9140.

105 W. L. Rauch and M. Liu, *J. Mater. Sci.*, 2003, **38**, 4307.

106 J.-C. Yang, J. V. Spirig, D. Karweik, J. L. Routbort, D. Singh and P. K. Dutta, *Sens. Actuators, B*, 2008, **131**, 448.

107 P. Dutta and J. C. Yang, *US Pat.*, US2007029210, 2007.

108 N. F. Szabo and P. K. Dutta, *Sens. Actuators, B*, 2003, **88**, 168.

109 N. F. Szabo, H. Du, S. A. Akbar, A. Soliman and P. K. Dutta, *Sens. Actuators, B*, 2002, **82**, 142.

110 J.-C. Yang and P. K. Dutta, *Sens. Actuators, B*, 2007, **125**, 30.

111 J.-C. Yang and P. K. Dutta, *J. Phys. Chem. C*, 2007, **111**, 8307.

112 S. P. Mondal, P. K. Dutta, G. W. Hunter, B. J. Ward, D. Laskowski and R. A. Dweik, *Sens. Actuators, B*, 2011, **158**, 292.

113 J.-C. Yang and P. K. Dutta, *Sens. Actuators, B*, 2007, **123**, 929.

114 G. Grubert, M. Stockenhuber, O. P. Tkachenko and M. Wark, *Chem. Mater.*, 2002, **14**, 2458.

115 K. Kaneyasu, K. Otsuka, Y. Setoguchi, S. Sonoda, T. Nakahara, I. Aso and N. Nakagaichi, *Sens. Actuators, B*, 2000, **66**, 56.

116 K. Tanaka, C.-K. Choo, S. Sumi, Y. Kamitani, T. Fujii, K. Satoh, K. Fukuda, R. Nakata, M. Yoshimune, Y. Yoshinaga and T. Okuhara, *J. Phys. Chem. B*, 2002, **106**, 4155.

117 D. P. Mann, T. Paraskeva, K. F. E. Pratt, I. P. Parkin and D. E. Williams, *Meas. Sci. Technol.*, 2005, **16**, 1193.

118 D. P. Mann, K. F. E. Pratt, T. Paraskeva, I. P. Parkin and D. E. Williams, *IEEE Sens. J.*, 2007, **7**, 551.

119 J. Trimboli and P. K. Dutta, *Sens. Actuators, B*, 2004, **102**, 132.

120 P. Yang, C. Lau, J.-Y. Liang, J.-Z. Lu and X. Liu, *Luminescence*, 2007, **22**, 473.

121 P. Yang, X. Ye, C. Lau, Z. Li, X. Liu and J. Lu, *Anal. Chem.*, 2007, **79**, 1425.

122 S. Konkayan, P. Chanthaanont, W. Prissanaroon, P. Hormnirun and A. Sirivat, *Mater. Technol.*, 2013, **28**, 332.

123 Y. Zheng, M. R. Mullen, J. Wang and P. K. Dutta, *Sens. Actuators, B*, 2014, **193**, 542.

124 L. Hu and L. Xuebao, *Shiyou Jiagong/Petrochem. Technol.*, 1999, **15**, 41.

125 R. Moos, *Int. J. Appl. Ceram. Technol.*, 2005, **2**, 401.

126 P. Chanthaanont and A. Sirivat, *Adv. Polym. Technol.*, 2013, **32**, 21367.

127 A. Sultana, D. D. Habermacher, C. E. A. Kirschhock and J. A. Martens, *Appl. Catal., B*, 2004, **48**, 65.

128 J. Zou, H. He, J. Dong and Y. Long, *J. Mater. Chem.*, 2004, **14**, 2405.

129 O. Schäf, V. Wernert, H. Ghobarkar and P. Knauth, *J. Electroceram.*, 2006, **16**, 93.

130 S. Mintova, J. Visser and T. Bein, *Stud. Surf. Sci. Catal.*, 2001, **135**, 360.

131 C. Baerlocher and L. B. McCusker, Database of Zeolite Structures, http://www.iza-structure.org/databases/.

132 G. Férey, *Chem. Soc. Rev.*, 2008, **37**, 191.

133 Y. Yu, J.-P. Ma and Y.-B. Dong, *CrystEngComm*, 2012, **14**, 7157.

134 I. A. Ibarra, T. W. Hesterberg, J.-S. Chang, J. W. Yoon, B. J. Holliday and S. M. Humphrey, *Chem. Commun.*, 2013, **49**, 7156.

135 I. A. Ibarra, T. W. Hesterberg, B. J. Holliday, V. M. Lynch and S. M. Humphrey, *Dalton Trans.*, 2012, **41**, 8003.

136 C.-C. Wang, C.-C. Yang, W.-C. Chung, G.-H. Lee, M.-L. Ho, Y.-C. Yu, M.-W. Chung, H.-S. Sheu, C.-H. Shih, K.-Y. Cheng, P.-J. Chang and P.-T. Chou, *Chem. – Eur. J.*, 2011, **17**, 9232.

137 T. Lee, Z. X. Liu and H. L. Lee, *Cryst. Growth Des.*, 2011, **11**, 4146.

138 I. Ellern, A. Venkatasubramanian, J. H. Lee, P. J. Hesketh, V. Stavila, M. D. Allendorf and A. L. Robinson, *ECS Trans.*, 2013, **50**, 469.

139 G. Lu, O. K. Farha, L. E. Kreno, P. M. Schoenecker, K. S. Walton, R. P. Van Duyne and J. T. Hupp, *Adv. Mater.*, 2011, **23**, 4449.

140 M. D. Allendorf, R. J. T. Houk, L. Andruszkiewicz, A. A. Talin, J. Pikarsky, A. Choudhury, K. A. Gall and P. J. Hesketh, *J. Am. Chem. Soc.*, 2008, **130**, 14404.

141 P. Davydovskaya, R. Pohle, A. Tawil and M. Fleischer, *Sens. Actuators, B*, 2013, **187**, 142.

142 A. Venkatasubramanian, J.-H. Lee, R. J. Houk, M. D. Allendorf, S. Nair and P. J. Hesketh, *ECS Trans.*, 2010, **33**, 229.

143 L. E. Kreno, J. T. Hupp and R. P. Van Duyne, *Anal. Chem.*, 2010, **82**, 8042.

144 J. Chen, J.-Y. Xu and Y. Chen, *Chin. Chem. Lett.*, 2013, **24**, 651.

145 P. Davydovskaya, A. Ranft, B. V. Lotsch and R. Pohle, *Anal. Chem.*, 2014, **86**, 6948.

146 R. Pohle, A. Tawil, P. Davydovskaya and M. Fleischer, *Procedia Eng.*, 2011, **25**, 108.

147 P. A. Szilágyi, R. J. Westerwaal, R. van de Krol, H. Geerlings and B. Dam, *J. Mater. Chem. C*, 2013, **1**, 8146.

148 S. Achmann, G. Hagen, J. Kita, I. M. Malkowsky, C. Kiener and R. Moos, *Sensors*, 2009, **9**, 1574.

149 R. Grünker, V. Bon, A. Heerwig, N. Klein, P. Müller, U. Stoeck, I. A. Baburin, U. Mueller, I. Senkovska and S. Kaskel, *Chem. – Eur. J.*, 2012, **18**, 13299.

150 Z. Hu, C. Tao, H. Liu, X. Zou, H. Zhu and J. Wang, *J. Mater. Chem. A*, 2014, **2**, 14222.

151 Y. Zhang, Y. Chen, Y. Zhang, H. Cong, B. Fu, S. Wen and S. Ruan, *J. Nanopart. Res.*, 2013, **15**, 2014.

152 J. An, C. M. Shade, D. A. Chengelis-Czegan, S. Petoud and N. L. Rosi, *J. Am. Chem. Soc.*, 2011, **133**, 1220.

153 Z. Xie, L. Ma, K. E. deKrafft, A. Jin and W. Lin, *J. Am. Chem. Soc.*, 2010, **132**, 922.

154 M.-L. Ho, Y.-A. Chen, T.-C. Chen, P.-J. Chang, Y.-P. Yu, K.-Y. Cheng, C.-H. Shih, G.-H. Lee and H.-S. Sheu, *Dalton Trans.*, 2012, **41**, 2592.

155 S. M. Barrett, C. Wang and W. Lin, *J. Mater. Chem.*, 2012, **22**, 10329.

156 X.-L. Qi, S.-Y. Liu, R.-B. Lin, P.-Q. Liao, J.-W. Ye, Z. Lai, Y. Guan, X.-N. Cheng, J.-P. Zhang and X.-M. Chen, *Chem. Commun.*, 2013, **49**, 6864.

157 R.-B. Lin, F. Li, S.-Y. Liu, X.-L. Qi, J.-P. Zhang and X.-M. Chen, *Angew. Chem., Int. Ed.*, 2013, **52**, 13429.

158 Z. Dou, J. Yu, Y. Cui, Y. Yang, Z. Wang, D. Yang and G. Qian, *J. Am. Chem. Soc.*, 2014, **136**, 5527.

159 X. Zou, J.-M. Goupil, S. Thomas, F. Zhang, G. Zhu, V. Valtchev and S. Mintova, *J. Phys. Chem. C*, 2012, **116**, 16593.

160 Y. Hwang, H. Sohn, A. Phan, O. M. Yaghi and R. N. Candler, *Nano Lett.*, 2013, **13**, 5271.

161 J. Ferrando-Soria, H. Khajavi, P. Serra-Crespo, J. Gascon, F. Kapteijn, M. Julve, F. Lloret, J. Pasán, C. Ruiz-Pérez, Y. Journaux and E. Pardo, *Adv. Mater.*, 2012, **24**, 5625.

162 G. Lu, O. K. Farha, W. Zhang, F. Huo and J. T. Hupp, *Adv. Mater.*, 2012, **24**, 3970.

163 G. Lu and J. T. Hupp, *J. Am. Chem. Soc.*, 2010, **132**, 7832.

164 E.-X. Chen, H. Yang and J. Zhang, *Inorg. Chem.*, 2014, **53**, 5411.

165 C. Cui, Y. Liu, H. Xu, S. Li, W. Zhang, P. Cui and F. Huo, *Small*, 2014, **10**, 3672.

166 L.-F. Song, C.-H. Jiang, C.-L. Jiao, J. Zhang, L.-X. Sun, F. Xu, W.-S. You, Z.-G. Wang and J.-J. Zhao, *Cryst. Growth Des.*, 2010, **10**, 5020.

167 P. Davydovskaya, V. Pentyala, L. Hussein, R. Pohle and G. Urban, in 2013 Transducers & Eurosensors XXVII: The 17th International Conference on Solid-State Sensors, Actuators and Microsystems (Tranducers & Eurosensors XXVII), IEEE, 2013, 2067.

168 P. Davydovskaya, V. Pentyala, O. Yurchenko, L. Hussein, R. Pohle and G. A. Urban, *Sens. Actuators, B*, 2014, **193**, 911.

169 Z. Hu, S. Pramanik, K. Tan, C. Zheng, W. Liu, X. Zhang, Y. J. Chabal and J. Li, *Cryst. Growth Des.*, 2013, **13**, 4204.

170 A. M. Marti, S. D. Perera, L. D. McBeath and K. J. Balkus, *Langmuir*, 2013, **29**, 5927.

171 K. Hirai, K. Sumida, M. Meilikhov, N. Louvain, M. Nakahama, H. Uehara, S. Kitagawa and S. Furukawa, *J. Mater. Chem. C*, 2014, **2**, 3336.

172 W.-J. Li, S.-Y. Gao, T.-F. Liu, L.-W. Han, Z.-J. Lin and R. Cao, *Langmuir*, 2013, **29**, 8657.

173 N. B. Shustova, A. F. Cozzolino, S. Reineke, M. Baldo and M. Dincă, *J. Am. Chem. Soc.*, 2013, **135**, 13326.

174 C. Zong, X. Liu, H. Sun, G. Zhang and L. Lu, *J. Mater. Chem.*, 2012, **22**, 18418.

175 O. S. Wolfbeis, *Anal. Chem.*, 2006, **78**, 3859.

176 S. K. Vashist and P. Vashist, *J. Sens.*, 2011, **2011**, 571405.

177 K. M. Goeders, J. S. Colton and L. A. Bottomley, *Chem. Rev.*, 2008, **108**, 522.

178 M. A. Schmidt and R. T. Howe, *Ceram. Eng. Sci. Proc.*, 1987, **8**, 1019.

179 C. A. Grimes, S. C. Roy, S. Rani and Q. Cai, *Sensors*, 2011, **11**, 2809.

180 S. W. James and R. P. Tatam, *Meas. Sci. Technol.*, 2003, **14**, R49.

181 F.-G. Banica, *Chemical Sensors and Biosensors: Fundamentals and Applications*, John Wiley & Sons, Chichester, 2012.

182 R. A. Potyrailo, C. Surman, N. Nagraj and A. Burns, *Chem. Rev.*, 2011, **111**, 7315.

183 M. Sabo, A. Henschel, H. Fröde, E. Klemm and S. Kaskel, *J. Mater. Chem.*, 2007, **17**, 3827.

184 J.-S. Choi, W.-J. Son, J. Kim and W.-S. Ahn, *Microporous Mesoporous Mater.*, 2008, **116**, 727.

185 M. E. Azim-Araghi and A. Krier, in *Selected Topics in Advanced Solid State and Fibre Optic Sensors*, ed. S. M. Vaezi-Nejad, IET, 2000, p. 215.

186 D. J. Wales, R. M. Parker, J. C. Gates, M. C. Grossel and P. G. R. Smith, *Sens. Actuators, B*, 2013, **188**, 857.

187 Q. M. Wang, D. Shen, M. Bülow, M. L. Lau, S. Deng, F. R. Fitch, N. O. Lemcoff and J. Semanscin, *Microporous Mesoporous Mater.*, 2002, **55**, 217.

188 D. Dou, M. Molinier and O. Bailey, *WO Pat.*, WO2001056686, 2001.

189 J. Schneider, C. Schnabel and J. Waldrop, *WO Pat.*, WO2005121763, 2005.

190 A. C. McKinlay, B. Xiao, D. S. Wragg, P. S. Wheatley, I. L. Megson and R. E. Morris, *J. Am. Chem. Soc.*, 2008, **130**, 10440.

191 N. J. Hinks, A. C. McKinlay, B. Xiao, P. S. Wheatley and R. E. Morris, *Microporous Mesoporous Mater.*, 2010, **129**, 330.

192 A. C. McKinlay, J. F. Eubank, S. Wuttke, B. Xiao, P. S. Wheatley, P. Bazin, J.-C. Lavalley, M. Daturi, A. Vimont, G. De Weireld, P. Horcajada, C. Serre and R. E. Morris, *Chem. Mater.*, 2013, **25**, 1592.

193 J. F. Eubank, P. S. Wheatley, G. Lebars, A. C. McKinlay, H. Leclerc, P. Horcajada, M. Daturi, A. Vimont, R. E. Morris and C. Serre, *APL Mater.*, 2014, **2**, 124112.

194 Z. Safidine, Z. Ghebache and S. Lamouri, *Polym. J.*, 2013, **45**, 946.

4320 | *Chem. Soc. Rev.*, 2015, **44**, 4290–4321

This journal is © The Royal Society of Chemistry 2015

195 I. G. Giannakopoulos, D. Kouzoudis, C. A. Grimes and V. Nikolakis, *Adv. Funct. Mater.*, 2005, **15**, 1165.

196 Y. Yan and T. Bein, *Chem. Mater.*, 1992, **4**, 975.

197 A. Fischerauer, G. Fischerauer, G. Hagen and R. Moos, *Phys. Status Solidi A*, 2011, **208**, 404.

198 A. Dubbe, *Phys. Status Solidi A*, 2011, **208**, 416.

199 G. Hagen and R. Moos, *Sens. Lett.*, 2011, **9**, 110.

200 I. Untea, D. Brasoveanu, M. Dancila and S. Bocskor, *Environ. Eng. Manage. J.*, 2002, **1**, 299.

201 D. Britt, D. Tranchemontagne and O. M. Yaghi, *Proc. Natl. Acad. Sci. U. S. A.*, 2008, **105**, 11623.

202 C. A. Fernandez, P. K. Thallapally, R. K. Motkuri, S. K. Nune, J. C. Sumrak, J. Tian and J. Liu, *Cryst. Growth Des.*, 2010, **10**, 1037.

203 T. G. Glover, G. W. Peterson, B. J. Schindler, D. Britt and O. Yaghi, *Chem. Eng. Sci.*, 2011, **66**, 163.

204 S. Yang, J. Sun, A. J. Ramirez-Cuesta, S. K. Callear, W. I. F. David, D. P. Anderson, R. Newby, A. J. Blake, J. E. Parker, C. C. Tang and M. Schröder, *Nat. Chem.*, 2012, **4**, 887.

205 K. Tan, P. Canepa, Q. Gong, J. Liu, D. H. Johnson, A. Dyevoich, P. K. Thallapally, T. Thonhauser, J. Li and Y. J. Chabal, *Chem. Mater.*, 2013, **25**, 4653.

206 X. Xu, J. Wang and Y. Long, *Microporous Mesoporous Mater.*, 2005, **83**, 60.

207 X.-W. Xu, J. Wang and Y.-C. Long, *Chin. J. Chem.*, 2005, **23**, 359.

208 S. J. Geier, J. A. Mason, E. D. Bloch, W. L. Queen, M. R. Hudson, C. M. Brown and J. R. Long, *Chem. Sci.*, 2013, **4**, 2054.

209 J. Caro and M. Noack, in *Advances in Nanoporous Materials*, ed. S. Ernst, Elsevier, Oxford, 2010, vol. 1, p. 1.

210 N. Mehio, S. Dai and D. Jiang, *J. Phys. Chem. A*, 2014, **118**, 1150.

211 P. Küsgens, M. Rose, I. Senkovska, H. Fröde, A. Henschel, S. Siegle and S. Kaskel, *Microporous Mesoporous Mater.*, 2009, **120**, 325.

212 J. Liu, P. K. Thallapally, B. P. McGrail, D. R. Brown and J. Liu, *Chem. Soc. Rev.*, 2012, **41**, 2308.

This journal is © The Royal Society of Chemistry 2015

Chem. Soc. Rev., 2015, **44**, 4290–4321 | 4321